nature communications

Article

https://doi.org/10.1038/s41467-025-56755-4

Transdermal microneedle-assisted ultrasound-enhanced CRISPRa system to enable sono-gene therapy for obesity

Received: 7 February 2024

Accepted: 29 January 2025

Published online: 10 February 2025

Check for updates

Shaoyue Li[1,2,3,4,5], Jifeng Yu[2,5], Yuting Shen[2,5], Bing Xiong[2], De Zhao[1,3,4], Weichen Xu[1,3,4], Shen Zhang[1,2,3,4], Xin Guan[2], Yunyun Liu[1,2,3,4], Xuexia Shan[1,3,4], Anqi Zhu[2], Qi Lyu[2], Yan Fang[2], Zitong Chen[2], Haohao Yin[2] ✉, Liping Sun[1,3,4] ✉ & Huixiong Xu[2] ✉

Obesity, a surging global health challenge, necessitates effective, accessible and innovative therapeutic models. Here we develop a spatiotemporally controllable microneedle (MN) drug delivery platform for sono-gene therapy to fight obesity. The platform delivers the methoxy polyethylene glycol-polyethyleneimine (mPEG-PEI) modified metal-organic frameworks (MOFs) sonosensitizer and the clustered regularly interspaced short palindromic repeats-activating (CRISPRa)/CRISPRa-uncoupling protein 1 (UCP1) system intradermally to adipocytes. Overall, this therapy platform is capable of achieving two major strategies of "annihilation" and "countermeasure": one is to kill redundant white adipocytes by sonodynamic therapy, and the other is to promote the browning of white adipocytes through the controllable release of CRISPRa-UCP1 system and sonodynamic effect. Obese male mice treated with this sono-gene therapy shows significant ameliorate in glucose tolerance and insulin sensitivity, successfully achieves weight loss and restrains weight rebound. This study may enable a standard treatment paradigm for sono-gene therapy of obesity and other metabolic diseases.

Obesity constitutes a global health priority due to its increasing prevalence and its association with various complications, including cardiovascular disease, type 2 diabetes mellitus, osteoarthritis, fatty liver, and several types of cancers (e.g., breast, colorectal, ovarian, liver, and pancreatic), accounting for the second most preventable causes of mortality worldwide[1–3]. Obesity is the condition of having an excessive accumulation of fat in adipose tissue, which is mainly divided into white adipose tissue (WAT) and brown adipose tissue (BAT) according to its location and function; the former can effectively store lipids while the latter generates heat by consuming lipids and glucose[4,5]. White adipocytes have been proposed as a major therapeutic target to combat obesity by inducing its browning due to its superficial location and accessibility[6,7]. Notably, brown adipocytes contain multiple mitochondria, which express unique thermogenic genes, with uncoupling protein 1 (*UCP1*) playing a central role[4]. *UCP1* uncouples oxidative phosphorylation from adenosine triphosphate (ATP) production to dissipate energy into heat, thereby combating obesity and related metabolic disorders[8]. Activation of *UCP1* expression has been shown to ac recruit *UCP1*-expressing beige adipocytes within WAT, increasing energy metabolism and thermogenesis for WAT browning[9]. UCP1-

[1]Department of Medical Ultrasound and Center of Minimally Invasive Treatment for Tumor, Shanghai Tenth People's Hospital, School of Medicine, Tongji University, Shanghai 200072, P. R. China. [2]Department of Ultrasound, Institute of Ultrasound in Medicine and Engineering, Zhongshan Hospital, Fudan University, Shanghai 200032, P. R. China. [3]Ultrasound Research and Education Institute, Clinical Research Center for Interventional Medicine, School of Medicine, Tongji University, Shanghai 200072, P. R. China. [4]Shanghai Engineering Research Center of Ultrasound Diagnosis and Treatment, Shanghai 200072, P. R. China. [5]These authors contributed equally: Shaoyue Li, Jifeng Yu, Yuting Shen. ✉e-mail: yin.haohao@zs-hospital.sh.cn; sunliping_s@126.com; xu.huixiong@zs-hospital.sh.cn

dependent thermogenesis is the most typical thermogenic effector used to induce browning of WAT, which is an effective way used to counteract the high calorie state of obesity[10,11]. Several reports have demonstrated the positive role of therapeutic strategies for post-transplantation overexpression of *UCP1* in the fight against obesity[12,13]. However, techniques for regulating genes that allow for sustainable overexpression of *UCP1* still have limitations that cannot be ignored, such as immunogenicity and genetic mutation[14].

The clustered regularly interspaced short palindromic repeats (CRISPR)/CRISPR-associated nuclease protein 9 (Cas9) system, including CRISPR-activating (CRISPRa) and CRISPR-interfering (CRISPRi) gene editing technologies, is a powerful tool for manipulating gene expression. It allows for stable long-term overexpression and knockdown of target genes with high efficiency and precision in gene editing, which has been widely adopted in the scientific community[15,16]. Subtypes of the activator system rely on the fusion of dead Cas9 (dCas9) with transcriptional activator structural domains (e.g., VP64 and KRAB), which together regulate gene expression for endogenous activation[17,18]. This technique has been used to activate the *UCP1* gene in mouse white preadipocytes[19,20]. Studies have shown that the dCas9 system has a lower risk of off-target effects compared to Cas9, and its action is relatively mild. However, it is worth noting that CRISPR-dCas9 technology is subject to degradation and immunoclearance of CRISPR systems, such as plasmid DNA (pDNA) and ribonucleoprotein (RNP), after direct delivery into the body during performing disease therapy[21]. Moreover, commonly used vectors like adeno-associated virus (AAV), lentivirus and lipid nanoparticles of non-viral vectors have limited loading capacity and systemic toxicity[22,23].

Metal-organic frameworks (MOFs) has become a promising option for delivering nucleic acid therapeutics due to its unique characteristics such as large surface area, customizable pore size, biocompatibility, and controlled degradation[24,25]. Some MOF materials have exhibited responsiveness to ultrasound (US), which can lead to the production of reactive oxygen species (ROS)[26]. Excessive ROS in WAT can trigger apoptosis of white adipocytes, potentially aiding in weight loss[27]. Besides, studies have highlighted that polyethylenimine (PEI) is recognized for its superior ability to induce transgene expression and is considered the "gold standard" for non-viral gene delivery[28]. While branched high molecular weight (HMW) PEI offers higher transfection efficiency, it also comes with increased cytotoxicity[28]. On the other hand, low molecular weight PEI (< 2 kDa) is less toxic but has reduced transfection efficiency. Covalent modification of polyethylene glycol (PEG) has been proposed as an effective approach to reduce this cytotoxicity[29].

Here, we report an intelligent spatiotemporally controllable ultrasound weight-loss microneedle (MN) patch that achieves sono-gene therapy against obesity by up-regulating the weight loss mobilizing gene while killing excess white adipocytes. As illustrated in Fig. 1, the zinc tetraphenyl(4-carboxyphenyl)porphyrin (Zn-TCPP) MOF, modified with methoxy polyethylene glycol (mPEG)/mPEG-PEI, is utilized as a carrier to load the CRISPRa-UCP1 plasmid (aUCP1) that upregulates *UCP1*. This loaded system is then encapsulated within hyaluronic acid (HA) microneedle (MN) patch to develop a US-controlled weight loss platform (MN-MP/aUCP1). The platform utilizes MNs' transdermal properties[30] to deliver the sono-gene modulation system (MP/aUCP1) to the subcutaneous fat layer and penetrate the adipocytes. mPEG-PEI (600 Da) modified Zn-TCPP exhibites HMW and cationic charge density that enables effective gene aggregation and endosomal escape. Furthermore, US irradiation can promote intracellular plasmid transfection and gene overexpression. In general, under the spatial and temporal control of US, on the one hand, it activates MOFs to efficiently generate ROS to kill excessive white adipocytes; and on the other hand, it enhances the expression of *UCP1* through the sonodynamic effect and stimulated the activation of *UCP1* within the CRISPRa-UCP1 system, which "counteracts" white fat to promote browning of WAT. The approach leads to a significant promotion of weight loss (18.3% ± 1.7% lost), improvement in insulin resistance, and long-term weight rebound restraint in mice. Additionally, the genome editing treatment triggered by the US substantially increases the level of oxidative stress in adipose tissue (e.g., 8OHdG), up-regulates the expression of browning-associated genes (e.g., *UCP1*), and down-regulates the expression of adipocyte markers (e.g., *Plin1*). This work presents a standard-of-care paradigm to combat obesity by spatiotemporally controllable sono-gene therapy strategy. This therapy shows promise for individuals with obesity and has potential applications in other metabolic-related diseases.

Results

MP/aUCP1 nanosystems preparation and characterization

Transmission electron microscopy (TEM) was used to observe the morphology and size of MOF (Zn-TCPP), which was in a lamellar structure with an average diameter of approximately 250 nm (Fig. 2a and Supplementary Fig. 1a). TEM elemental mapping revealed that the elements of carbon (C), nitrogen (N), oxygen (O), and zinc (Zn) were evenly distributed throughout the structure of the metal-organic framework (Zn-TCPP) structure (Fig. 2a). To further verify the elemental composition and valence states of Zn-TCPP nanosheets, X-ray photoelectron spectroscopy (XPS) was performed. The main composition of the elements was found to be in agreement with the result observed in the mapping images (Fig. 2b). Furthermore, the Zn 2*p* exhibited two distinct peaks, confirming the presence of Zn valence state in Zn-TCPP nanosheets. The optical properties of Zn-TCPP nanosheets were examined using ultraviolet-visible (UV-vis) spectroscopy (Fig. 2c). The free TCPP exhibited a characteristic peak of porphyrin ring at 425 nm, while the characteristic peak of Zn-TCPP nanosheets showed a slight red shift (435 nm), which was consistent with previous literature reports[31]. The TCPP molecule in its free form exhibited within the range of 510–650 nm, whereas the Zn-TCPP nanosheets displayed two Q-bands at 558 and 595 nm, respectively, indicating successful metallization of the porphyrin rings by the Zn^{2+} ions (Fig. 2c). The binding mode of porphyrin with Zn atoms was further investigated by fourier transform infrared spectroscopy (FT-IR) (Fig. 2d). In the spectrum of TCPP, the absence of the C = O stretching vibration peak at ≈1700 cm^{-1} implied a change in the carboxyl group of the porphyrin. Additionally, two new peaks emerged in the spectrum of Zn-TCPP at ≈1600 and 1400 cm^{-1}, suggesting that the carboxyl group in the TCPP ligands to the metal to form Zn-O bonds. Furthermore, the planar vibration of N-H disappeared at 982 cm^{-1} and a new peak emerged at 995 cm^{-1}, suggesting that Zn-TCPP belongs to the metal porphyrin[32].

A CRISPRa-UCP1 plasmid was constructed to edit the uncoupling protein gene by cloning single guide RNA (SgRNA) targeting *UCP1* and stably expressed vector encoding dCas9 fused with VPR. The fusing protein contained the viral protein 16 transcriptional activator (VP64), the NF-κB transactivating subunit p65, and the Epstein-Barr virus R trans-activator (Rta) (VP64-p65-Rta) (Fig. 2e). It was confirmed that UCP1 expression was elevated in mature adipocytes transduced with aUCP1 in comparison to control groups (Fig. 2f). The binding affinity between mPEG-PEI modified MOFs (MP) and aUCP1 was studied by agarose gel electrophoresis assay (Fig. 2g). The findings indicated that as the amount of aUCP1 increases, the MP capacity became inadequate. To enhance transfection efficiency and shield the plasmid from nuclease degradation, MP was effectively bound with aUCP1 at a mass ratio of 4:1. TEM analysis revealed an increase in C, N, and O elements in MP/aUCP1, indicating successful modification of mPEG-PEI. And the presence of phosphorus (P) elements further confirmed the successful loading of aUCP1 in MP (Fig. 2a and Supplementary Fig. 1b). Additionally, the zeta potential changed from negative to positive after mPEG-PEI modification (Fig. 2h). Subsequently, MP was used to load aUCP1 through by electrostatic adsorption, and the final average zeta potential of MP/aUCP1 was measured to be 3.39 mV (Fig. 2h). Dynamic

https://doi.org/10.1038/s41467-025-56755-4

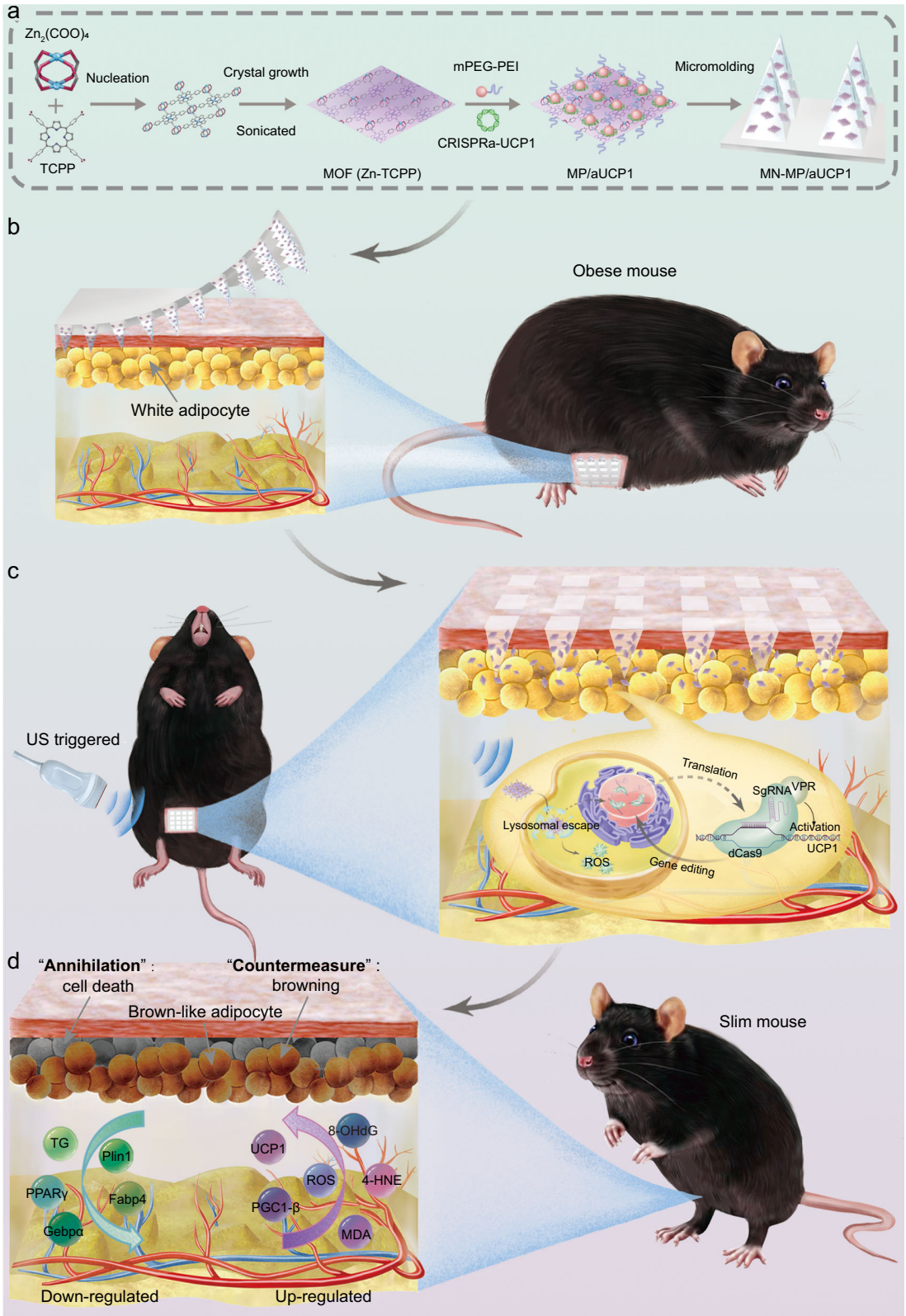

Fig. 1 | Preparation process of MN-MP/aUCP1 and its application in anti-obesity therapy based on spatiotemporally controllable sono-gene therapy platform. **a** Schematic illustration for synthesis process of MN-MP/aUCP1 patch. **b** MN-MP/aUCP1 patch was inserted into white adipose tissue in the inguinal groin of obese mice. **c** The spatiotemporally controllable release of MP/aUCP1 from MN patch under US irradiation. **d** "Annihilation" and "countermeasure": apoptosis and browning of white adipocytes. MN, microneedle; US, ultrasound.

https://doi.org/10.1038/s41467-025-56755-4

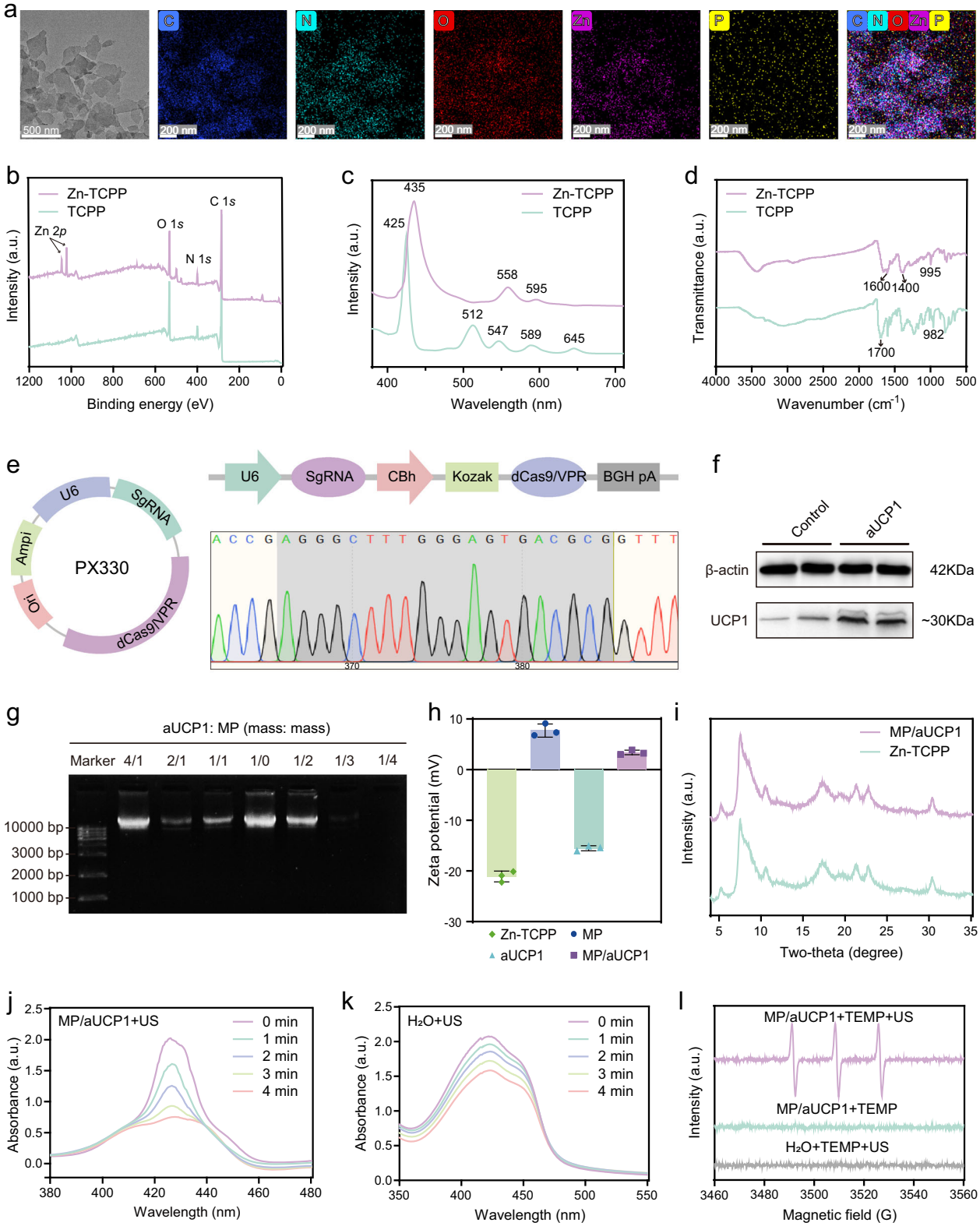

Fig. 2 | Characterization and singlet oxygen-generating capacity of MP/aUCP1 nanosystems. a TEM image and corresponding element mappings of Zn-TCPP nanosheets. **b** XPS survey scan of TCPP and Zn-TCPP nanosheets. **c** UV-vis absorption spectra of TCPP and Zn-TCPP nanosheets. **d** FT-IR spectra of TCPP and Zn-TCPP. **e** Schematic of PX330 vector with SgRNA inserted and sequencing result of SgRNA targeting *UCP1* in CRISPRa-UCP1 plasmid. **f** Protein expression of UCP1 in mature adipocytes after co-incubation with or without aUCP1. **g** Agarose gel electrophoresis of MP/aUCP1 at different mass ratios (aUCP1: MP = 4: 1, 2: 1, 1: 1, 1: 0, 1: 2, 1: 3, 1: 4). **h** Zeta potentials of Zn-TCPP, MP, aUCP1, and MP/aUCP1. Data are given as means ± standard deviation (SD) ($n = 3$ independent samples). **i** XRD patterns of Zn-TCPP and MP/aUCP1. **j, k** UV-vis absorbance spectrum of DPBF with addition of MP/aUCP1 (50 μg mL^{-1}) (j) or H_2O (k) under US irradiation. **l** Electron spin resonance (ESR) measurements of US only, MP/aUCP1, and MP/aUCP1 + US. The experiments for **a**–**d**, **f**, **g**, and **i**-**l** were repeated three times independently with similar results. Source data are provided as a Source Data file.

light scattering (DLS) measurements demonstrated that loading with aUCP1 increased the average size of the MP from 257.1 nm to 288 nm (Supplementary Fig. 1c). As the X-ray diffraction (XRD) illustrated, MP/aUCP1 nanosystems retained good crystallinity despite the loading of mPEG-PEI and aUCP1, indicating that the crystal structure was not significantly affected (Fig. 2i). The above results indicated the successful co-loading of mPEG-PEI and aUCP1.

Sonodynamic property and in vitro anti-obesity performance of MP/aUCP1 nanosystems

To further investigate the sonodynamic properties of the MP/aUCP1 nanosystems, UV-visible spectroscopy and electron spin resonance (ESR) spectroscopy were used to detect the production of ROS. The yield of singlet oxygen ($^1O_2$) detected using DPBF as a probe significantly increased with the duration of the ultrasonic stimulation (Fig. 2j and Supplementary Fig. 2a), confirming the desirable properties of the nanosystems. However, pure H_2O exhibited an unsatisfactory increase in $^1O_2$ after ultrasonic irradiation (Fig. 2k and Supplementary Fig. 2a). In addition, $^1O_2$ was captured using 2,2,6,6-tetramethylpiperidine (TEMP). The characteristic signals (1:1:1) of $^1O_2$ were identified in the MP/aUCP1 + US group, in comparison to the US and MP/aUCP1 group (Fig. 2l). Flow cytometry (FCM) analysis and confocal laser scanning microscopy (CLSM) were used to test the capacity to produce ROS of MP/aUCP1 in fully developed 3T3-L1 preadipocytes. As shown in Fig. 3a, b and Supplementary Fig. 2b, the average levels of ROS within mature adipocytes were 50.8% and 50.4% in the MP + US group and the MP/aUCP1 + US group, respectively. These levels were significantly higher than those observed in the control groups. Similarly, the results obtained from CLSM using the 2,7-dichlorofluorescein diacetate (DCFH-DA) probe were consistent with those from the FCM analysis, confirming that MP/aUCP1 was capable of producing significant intracellular ROS upon US stimulation (Fig. 3c and Supplementary Fig. 2c).

Then, the anti-obesity effect was assessed in vitro. The results, as shown in Supplementary Fig. 2d and Fig. 3d, indicated that MP/aUCP1 had high biosafety, with negligible cytotoxicity to 3T3-L1 preadipocytes and mature adipocytes even at higher concentrations. Following incubation with MP/aUCP1, both 3T3-L1 preadipocytes and mature adipocytes showed a sonodynamic therapy (SDT) effect that was dependent on power density when exposed to US irradiation (Supplementary Fig. 2e and Fig. 3e). To further validate the therapeutic potential of the nanosystems, the viability of mature adipocytes after different treatments was detected using FCM. The MP/aUCP1 + US group showed a significantly higher rate of apoptosis (43.5%) compared to other treatments (Supplementary Fig. 2f and Fig. 3f). Consistently, the killing effect was also observed in 3T3-L1 preadipocytes (Supplementary Fig. 2g). Simultaneously, the study evaluated the therapeutic effect of various treatments on triglyceride (TG) storage in adipocytes. The results showed that mature adipocytes co-incubated with MP/aUCP1 exhibited a remarkable decrease in intracellular TG after US irradiation, implying that MP/aUCP1 effectively inhibited lipid storage (Fig. 3g).

Efficient lysosomal escape and gene editing capabilities of MP/aUCP1 nanosystems in vitro

CLSM was utilized to investigate the cellular uptake capability of FITC-labeled MP/aUCP1. The P/aUCP1 group (synthesized by mPEG-PEI wrapped aUCP1) and the aUCP1 group (using commercially available Lipofectamine 2000 as a transfection aid) served as control groups. The findings indicated that mature adipocytes effectively internalized MP/aUCP1, with US enhancing the cellular enrichment of MP/aUCP1 (Supplementary Fig. 3a). Efficient escape from lysosomes post-endocytosis is crucial for gene editing. As depicted in Supplementary Fig. 3b, MP/aUCP1 nanosystems successfully evaded lysosomes after 4 h of incubation, primarily attributed to the "proton sponge" effect induced by PEI in MP/aUCP1[28]. Importantly, this endosomal escape effect was more pronounced under US irradiation, validating that US irradiation enhanced the genome editing potential of the MP/aUCP1 nanosystems.

Next, the transfection efficiency of MP/aUCP1 in cells was studied following US irradiation. A plasmid encoding enhanced green fluorescent protein (pEGFP), similar in size to the CRISPRa-UCP1 plasmid, was chosen as a reporter gene. FCM analysis revealed that MP/aUCP1 transfected over 50% of 3T3-L1 preadipocytes and mature adipocytes, with a transfection efficiency approximately 3 times higher than that of P/aUCP1, and comparable to Lipofectamine 2000 (group aUCP1@EGFP) (Supplementary Fig. 4). In addition, following US irradiation, the cell transfection rate exceeded 60% (Supplementary Fig. 4). Similarly, fluorescence microscopy confirmed consistent results (Supplementary Fig. 5). These results indicated that MP/aUCP1 nanosystems significantly increased US-mediated plasmid transfection.

Fabrication and characterization of the MN-MP/aUCP1 patch

Intelligent MN patch was created using a micromolding method in which 15 wt% HA solution was mixed with MP/aUCP1 solution and placed into a polydimethylsiloxane (PDMS) mold. The mold was then vacuum processed, after which 15 wt% HA solution was cast into the micromold. The resulting product was dried at room temperature and demolded (Fig. 4a). As shown in Fig. 4b and Supplementary Fig. 6a, the MN patch had dimensions of 1 cm × 1 cm, with a 12-by-12 MN array. Each needle was molded in a pyramid shape with a base diameter of 300 μm and a height of 800 μm. The color of MNs loaded with MP/aUCP1 were deepened, while scanning electron microscopy (SEM) images indicated that loading drugs did not affect the successful synthesis of MN (Fig. 4c, d). The mechanical strength of patches made from 10 wt%, 15 wt% or 20 wt% HA solution was determined using a tensile testing machine (Fig. 4e). The smoothing continuous force-displacement curves disclosed that no microneedle fractured during compression. Additionally, the 15 wt% MN patch exhibited excellent mechanical properties, providing sufficient stiffness to penetrate the skin compared to the 10 wt% patch, and had a substantially higher minimum average force required for skin penetration (0.058 N) (Fig. 4e). The hematoxylin and eosin (H&E) staining clearly depicted the MNs going through the epidermis into the dermis (Fig. 4f). The patches were applied to the skin of obese mice in the inguinal region and the MNs were completely dissolved in the skin after 15 minutes, with no evident skin irritation or damage at the site of administration (Fig. 4g). There was no apparent inflammatory response discovered in the region where the patch was pressed, as compared with the unpatch-treated skin tissue (Supplementary Fig. 6b).

MN patches with different amounts of MP/aUCP1 were manufactured and tested. Increasing the MP/aUCP1 content from 50 μg to 200 μg led to a change in the MNs' stiffness (Supplementary Fig. 6c). Interestingly, MN patches with 100 μg MP/aUCP1 exhibited similar mechanical strength to those with 50 μg MP/aUCP1 and were able to penetrate the skin smoothly (Supplementary Fig. 6c and Supplementary Fig. 6d). Therefore, MN patches loaded with 100 μg MP/aUCP1 were chosen for further investigations. FCM analysis revealed a slight improvement in cell transfection rates when utilizing HA MN patches for drug delivery (Supplementary Fig. 6e). Figure 4h exhibited the fluorescence images of representative MN patches containing MP/Cy3 and aUCP1-ICG, where loaded MP nanosheets and CRISPRa system were evenly distributed inside the MNs. Moreover, there was no notable redness observed in the MN-MP/aUCP1 treated group after 1 day, in comparison to the control group and skin injected with MP/aUCP1 (Supplementary Fig. 6f). The drug-carrying patch's biodistribution and ability to target WAT were monitored using the in vivo imaging system (IVIS) spectrum imaging system. Clearly, in vivo fluorescence imaging confirmed that aUCP1 remained present for one day under condition without MN encapsulation, whereas MP-wrapped aUCP1 injection (InJ) continued to be visible subcutaneously in obese

https://doi.org/10.1038/s41467-025-56755-4

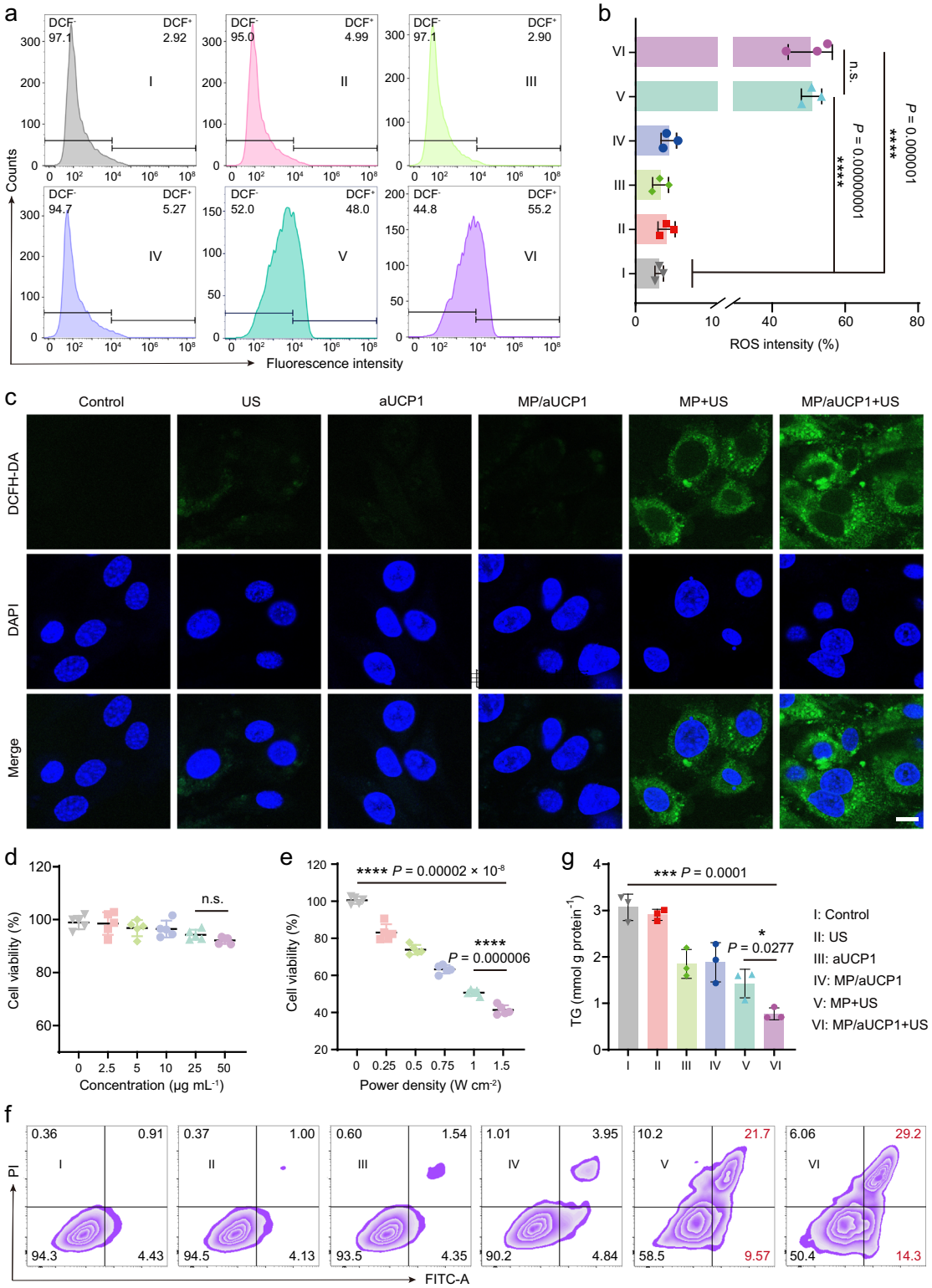

Fig. 3 | Sonodynamic property of MP/aUCP1 nanosystems. FCM analysis of ROS levels (**a**) in mature 3T3-L1 adipocytes and corresponding fluorescence intensity (**b**) after various treatments. Data are given as means ± SD ($n = 3$ biologically independent samples). For the gating strategy, seen in the Supplementary Fig. 2b. **c** CLSM observation of mature adipocytes stained with DCFH-DA and after different treatments (Scale bar: 10 μm). **d** Viability of mature adipocytes post coculture with different concentrations (0, 2.5, 5, 10, 25, and 50 μg mL^{-1}) of MP/aUCP1 nanosystems for 24 h. Data are presented as means ± SD ($n = 5$ biologically independent samples). **e** Mature adipocytes viability treated with MP/aUCP1 (50 μg mL^{-1}) plus various power densities (0, 0.25, 0.5, 0.75, 1, and 1.5 W cm^{-2}) of US irradiation. Data are presented as means ± SD ($n = 5$ biologically independent samples). **f** Flow cytometric apoptosis analysis of mature adipocytes in different groups. For the gating strategy, seen in the Supplementary Fig. 2f. **g** Cellular triglyceride concentrations post different treatments. Data are presented as means ± SD ($n = 3$ biologically independent samples). I: control, II: US irradiation, III: aUCP1, IV: MP/aUCP1, V: MP + US irradiation, VI: MP/aUCP1 + US irradiation. The experiments for **c** and **f** were repeated three times independently with similar results. Statistical differences for **b**, **d**, **e**, and **g** were calculated using two-tailed unpaired student's *t*-test. n.s., not significant, $^{*}P < 0.05$, $^{***}P < 0.001$, and $^{****}P < 0.0001$. Source data are provided as a Source Data file.

https://doi.org/10.1038/s41467-025-56755-4

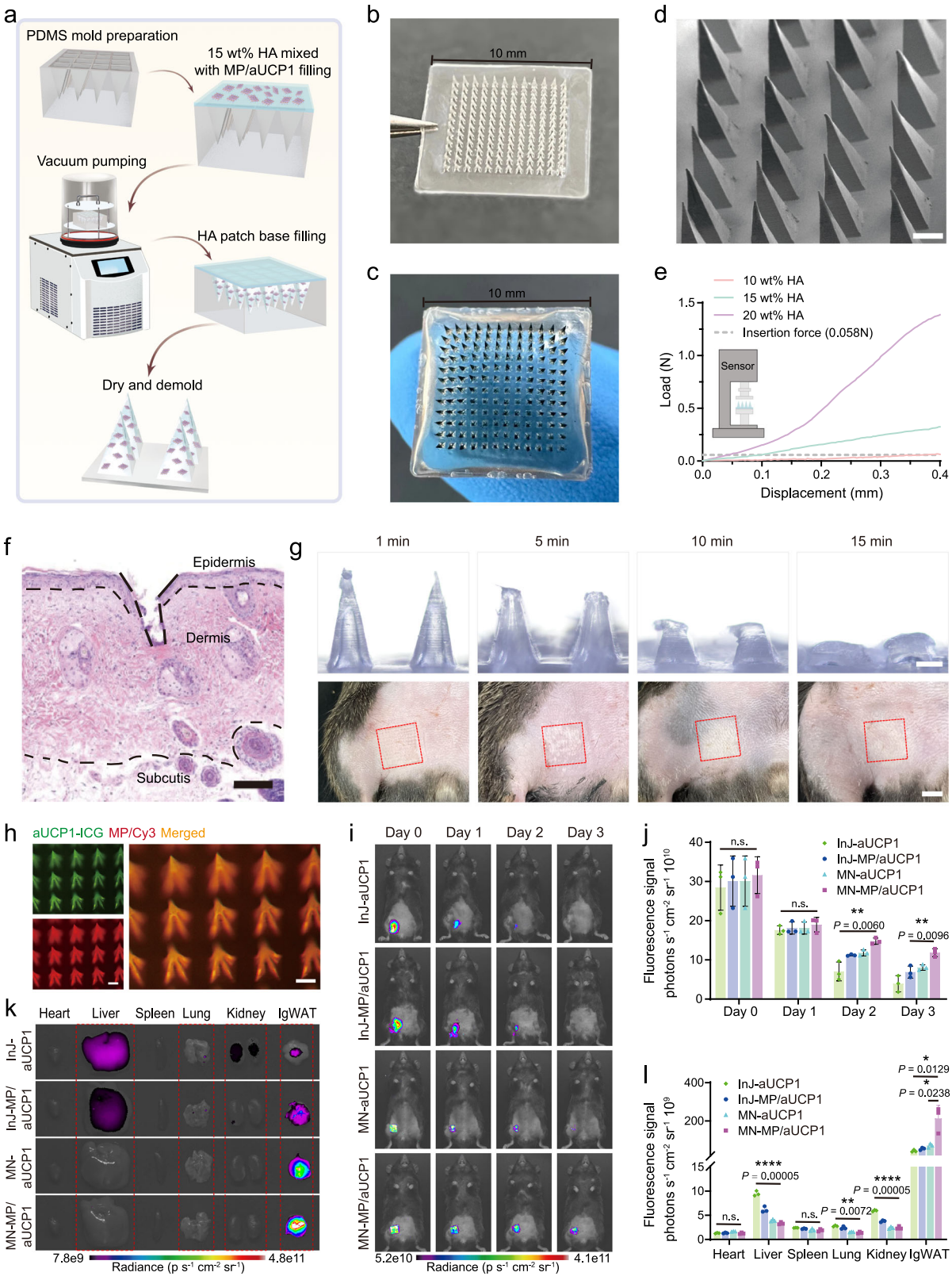

mouse until the second day (Fig. 4i). Compared to MN-aUCP1-treated mouse, MN-MP/aUCP1-treated mouse still had considerably higher fluorescence signal on the third day (Fig. 4i, j). Analysis of the distribution of ex vivo organs within 3 days of treatment revealed that relatively fewer fluorescent signals were retained in organs such as the livers, lungs, and kidneys in all groups. In contract, mice treated with MN administration exhibited higher signal intensity within inguinal WAT (IgWAT) (Fig. 4k, l and Supplementary Fig. 6g–i). Taken together, these findings suggested that MN patch improved the long-term retention of MP/aUCP1 in WAT.

Anti-obesity effect of MN-MP/aUCP1 + US

The potential of intelligent drug-loading patches for treatment of obesity in mice was evaluated. To model obesity, C57BL/6 J male mice

Fig. 4 | Fabrication and characterization of the MN-MP/aUCP1 patch. **a** Schematic illustration of MN patch fabrication. Representative digital photographs of MN patch (**b**) and MP/aUCP1 loaded MN patch (**c**). **d** SEM image of the MN-MP/aUCP1 patch (Scale bar: 200 μm). **e** Mechanical strength of the MN patches with different concentrations of HA and schematic diagram of the corresponding testing device. **f** H&E staining of mouse skin exhibits penetration of single MN (Scale bar: 100 μm). **g** Top: demonstration of the MN tips pressed into the skin for different times (Scale bar: 200 μm). Bottom: Skin recovery after MN treatment showing slight irritation (Scale bar: 5 mm). **h** Fluorescence images of MN patch containing aUCP1-ICG and Cy3-loaded MP nanosheets (Scale bars: 200 μm). **i** In vivo fluorescence images of aUCP1 (aUCP1-ICG) and MP/aUCP1 (MP loaded aUCP1-ICG) delivered by subcutaneous injection (InJ) or MN patches inserting in the inguinal region. **j** Quantification of fluorescence intensity during the 3-day treatment period. Data are presented as means ± SD ($n = 3$ mice per group). Ex vivo organ fluorescence biodistribution (**k**) and corresponding fluorescence intensity quantitative analysis in organs (**l**) explanted from mice at 24 h after subcutaneous InJ or MN patches delivery of aUCP1 and MP/aUCP1. Data are presented as means ± SD ($n = 3$ biologically independent samples). The experiments for **d**–**g** and **h** were repeated three times independently with similar results. Statistical differences for **j** and **l** were calculated using two-tailed unpaired student's *t*-test. n.s., not significant, $^{*}P < 0.05$, $^{**}P < 0.01$, and $^{****}P < 0.0001$. Source data are provided as a Source Data file.

(6–8 weeks old, ≈18 g) were feed a high-fat diet (HFD) for approximately 8 weeks until they reached ≈35 g body weight (Fig. 5a). Given the abundance of WAT in the inguinal region of mice and its superficial position, MN patches were implanted in the IgWAT of mice for anti-obesity treatment. The mice were randomly assigned to one of six groups for different treatments: I) control, II) MN + US irradiation, III) MN-aUCP1, IV) MN-MP/aUCP1, V) MN-MP + US irradiation, and VI) MN-MP/aUCP1 + US irradiation. The anti-obesity treatment was divided into seven sessions of MN patch injections every three days, followed by irradiation of mice at the inguinal region with US 15 min after the MN patch injection (Fig. 5a). During the 21-day anti-obesity treatment, food intake and body weight were monitored every three days. Despite similar high-fat dietary intake in all groups of mice, mice in the control and US-only groups gained 8.2 ± 2.2% (from 34.6 ± 1.0 to 37.4 ± 0.8 g) and 8.3 ± 1.6% (from 34.4 ± 0.8 to 37.3 ± 0.9 g) of body weight, respectively (Fig. 5b, c and Supplementary Fig. 7a). In contrast, the MN-MP/aUCP1 + US and MN-MP + US groups, lost 18.3% ± 1.7% and 13.4% ± 3.2% of their body weight, respectively. Treatment with MN-MP/aUCP1 without US irradiation resulted in a decrease in body weight of 6.9% ± 2.1% the mice, which was similar to that in the MN-aUCP1 group (loss in body weight of 8.3% ± 2.3%) (Fig. 5b, c and Supplementary Fig. 7a). In addition, the mice in the MN-MP + US and MN-MP/aUCP1 + US groups exhibited a reduction in body fat and a leaner physique, as evidenced by the digital photographs of the mice taken at the end of the treatment (Fig. 5d). Subsequently the mice were sacrificed and IgWAT, perigonadal WAT (PgWAT) and perirenal WAT (PrWAT) were dissected out for size and mass comparison. Both subcutaneous and visceral WAT were smaller in volume and lower in mass in the MN-MP/aUCP1 + US group compared with the other groups (Fig. 5e, f).

H&E staining of isolated fats further supported that the MN-MP/aUCP1 + US treatment regimen not only substantially shrunk the adipocytes in IgWAT, but also in PgWAT and PrWAT, indicating that this treatment was not limited to subcutaneous inguinal fat but caused systemic fat reduction (Fig. 5g, h). Impressively, the H&E staining of the livers of mice using the sono-gene treatment strategy appeared a dramatical reduction in fat content compared to those in the control and MN + US groups (Fig. 5i), accompanied by a marked reduction in liver morphology (Supplementary Fig. 7b). Corresponding oil red O staining demonstrated that the CRISPRa-UCP1 system had the ability to effectively alleviate fatty liver comorbidity. The addition of the US irradiation further enhanced the anti-obesity treatment effect (Fig. 5i).

Monitor of weight regain after MN-MP/aUCP1 + US treatment

Maintaining body weight after weight loss is a major challenge in obesity management. To validate the durability and efficacy of the US-triggered CRISPRa-UCP1 system for anti-obesity treatment, mice were monitored for high-fat intake and weight regain after seven courses of treatment over a 21-day period (Fig. 5a). During the 15-day monitoring period, all groups of mice consumed nearly equal amounts of food (Fig. 5j). However, the mice in the MN-MP/aUCP1 + US group exhibited the lowest weight gain compared to all the other groups at the end of the observation period (Fig. 5k, l, Supplementary Fig. 7c). Taken together, these results provided exciting evidence that the strategy of US-triggered genome editing therapy potently reduced body weight in obese mice as well as markedly inhibited weight rebound.

MN-MP/aUCP1 + US treatment facilitates thermogenesis and metabolism in HFD induced obese mice

Following the confirmation of the anti-obesity effects of MN-MP/aUCP1 + US, we conducted a more detailed investigation into the physiological impacts of this treatment. Metabolic physio-cage study was performed during the final days of the treatment experiments on obese mice. During the dark cycle, mice in the MN-MP/aUCP1 and MN-MP/aUCP1 + US treatment groups exhibited increased oxygen consumption and elevated heat production (Fig. 6a and Supplementary Fig. 8a–c). Notably, there were no significant changes in the activity levels or food intake of the mice (Supplementary Fig. 8d, e). These results supported the conclusion that MN-MP/aUCP1 + US treatment mitigated obesity by enhancing energy expenditure. Strikingly, mice treated with MN-MP/aUCP1 ($P < 0.001$) and sono-gene therapy ($P < 0.0001$) both showed enhanced cold tolerance, as evidenced by their ability to maintain a higher core body temperature when exposed to cold (Fig. 6b). Furthermore, compared with the control group, a more pronounced increase in energy expenditure was observed following adrenergic stimulation via CL-316,243 injection (Fig. 6c, d and Supplementary Fig. 9a). Collectively, these findings indicated that MN-MP/aUCP1 + US significantly enhanced the thermogenic capacity of the treated mice. Besides, the mice treated with MN-MP/aUCP1 + US gained lower circulating glucose and insulin levels compared those to the control group, resulting in significant improvements in insulin resistance and glucose tolerance (Fig. 6e–g and Supplementary Fig. 9b). Plasma chemistry analysis consistently showed a decreasing trend in TG and cholesterol levels, along with an increase in free fatty acids (FFA) produced by lipolysis, when treated with MN-MP/aUCP1 plus US enhancement (Supplementary Fig. 9c–e).

To determine whether the metabolic benefits observed in chronically treated mice were directly attributable to MN-MP/aUCP1 + US or were instead related to reductions in body weight and fat mass, we conducted daily treatments on mice for a duration of three days. During this acute treatment period, no significant differences in body weights were noted between the treated and control groups (Supplementary Fig. 10a). When the body weights of mice in each group were matched, metabolic physio-cage study was conducted using mice on day 3 after treatment (Supplementary Fig. 10a). Notably, the oxygen consumption and caloric expenditure of the acute MN-MP/aUCP1 + US-treated mice exhibited a significant upward trend (Supplementary Fig. 10b–e). The activity levels, food intake, and core body temperatures across all groups remained similar (Supplementary Fig. 10f–h). Importantly, norepinephrine (NE) levels in both serum and IgWAT, cortisol levels in serum, and thermogenesis in BAT did not show significant changes following treatment (Supplementary Fig. 11a–e). These results indicated that sono-gene therapy did not significantly alter systemic or local stress hormone production, thereby ruling out the possibility that the observed increase in thermogenesis was due to heightened adrenergic stimulation. Collectively, these data suggested

https://doi.org/10.1038/s41467-025-56755-4

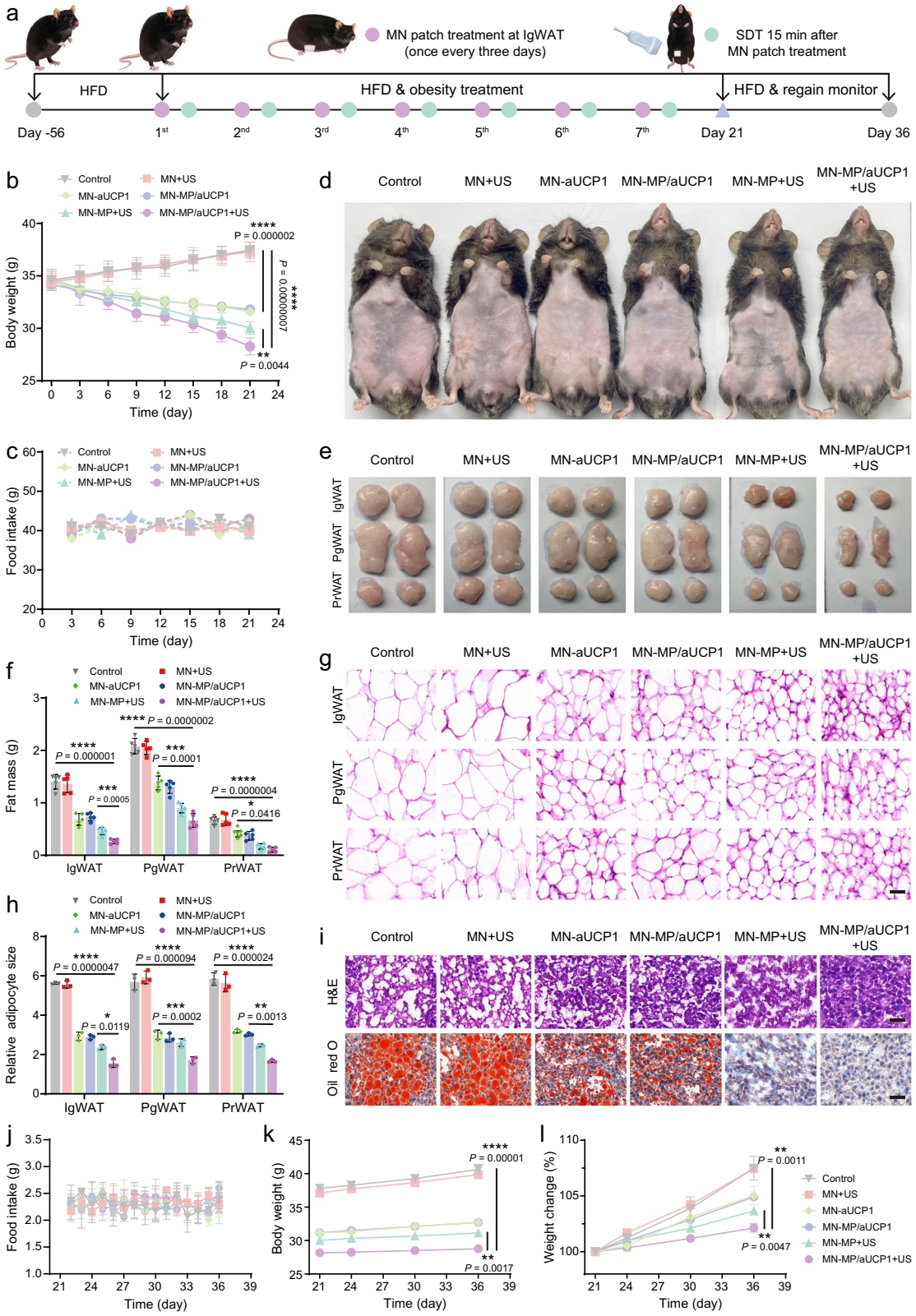

that MN-MP/aUCP1 + US may ameliorate obesity and related metabolic disorders by activating IgWAT thermogenesis and improving metabolic levels.

In addition, we evaluated the biosafety of this sono-gene therapy strategy for obesity. Encouragingly, our anti-obesity treatment regimen did not show any damage to major organs (Supplementary Fig. 12). Blood routine, cardiac function and serum biochemical results of mice also proved that the treatment had no potential toxic side effects (Supplementary Figs. 13, 14). It is worth noting that the control groups (Control and MN + US) exhibited increases in the circulating amounts of alanine transaminase (ALT) and aspartate transamine (AST). In contrast, the levels of these enzymes in the other groups remained within the normal ranges. This may be attributed to fatty liver symptoms in the control groups. Sonodynamic oxidative damage

Fig. 5 | The anti-obesity treatment and long-term benefit with MN-MP/aUCP1 patch under US irradiation. a Schematic illustration for different treatments of mice. **b** Changes in body weight of mice at different treatment conditions. Data are presented as means ± SD ($n = 5$ mice per group). **c** Total intake of HFD in each group of mice under different treatment conditions ($n = 5$ mice per group). **d** Representative obese mice photographs on the 21st day of various treatments as indicated. **e** Representative photographs of various isolated adipose tissues extracted from mice in (d). **f** Weight of the extracted adipose tissue. Data are presented as means ± SD ($n = 5$ biologically independent samples). **g** Representative H&E images from different parts and different groups of adipose tissues (Scale bar: 50 μm). **h** Corresponding morphometric analysis of the adipocyte size. Data are presented as means ± SD ($n = 3$ biologically independent samples). **i** H&E and oil red O stained observation of liver sections isolated from mice after 21 days of different treatments (Scale bar: 50 μm). **j** Daily diet intake of different treated mice during the 15-day weight recovery monitoring segment. Data are presented as means ± SD ($n = 3$ mice per group). Change of body weight (**k**) and the corresponding percentage of weight change (**l**) during the following 15 days after treatment at various conditions. Data are presented as means ± SD ($n = 3$ mice per group). The experiments for **g** and **i** were repeated three times independently with similar results. Statistical differences for **b, f, h, k**, and **l** were calculated using two-tailed unpaired student's *t*-test. $^{*}P < 0.05$, $^{**}P < 0.01$, $^{***}P < 0.001$, and $^{****}P < 0.0001$. Source data are provided as a Source Data file.

may trigger a robust inflammatory response, further exacerbating obesity-induced fibrosis of the liver and adipose tissue[33]. To evaluate the extent of damage, levels of serum and adipose inflammatory cytokines were measured, and the degree of fibrosis in the liver and adipose tissue was assessed. Fortunately, enzyme-linked immunoassay (ELISA) testing of mice serum and IgWAT revealed that MN-M/aUCP1+US treatment did not stimulate the production of inflammatory cytokines such as IL-1β, IL-6, and TNF-α (Supplementary Fig. 15). Moreover, US irradiation did not lead to a significant increase in the degree of fibrosis in the liver and adipose tissue (Fig. 6h, i). Therefore, these data suggested that this sono-gene therapeutic strategy held great promise for biosecurity.

Alterations at the molecular level of IgWAT after MN-MP/aUCP1 + US treatment

To better evaluate the efficacy of MN-MP/aUCP1-mediated sono-gene therapy, the role of US-induced genome editing systems was investigated in obese mice at a molecular level. Terminal deoxynucleotidyl transferase-mediated dUTP nick-end labelling (TUNEL) revealed a significant increase in apoptotic cells in IgWAT, PgWAT, and PrWAT of mice treated with MN-MP/aUCP1 + US compared to MN-MP + US, with the most pronounced effect observed in IgWAT (Fig. 7a, Supplementary Fig. 16a). This study suggested that the apoptosis of adipocytes is largely due to oxidative stress induced by the sonodynamic reaction, which caused the accumulation of ROS accumulate in the cytoplasm and organelles, damaging lipids, proteins, and DNA, ultimately leading to cell death[33]. To demonstrate this point, the levels of adipose ROS, lipid peroxidation products (malondialdehyde (MDA), 4-hydroxynonenal (4-HNE)), and DNA oxidation products (8-hydroxy-2′-deoxyguanosine (8-OHdG)) were examined. As anticipated, ROS levels were significantly increased in the MN-MP + US group and the MN-MP/aUCP1 + US group (Fig. 7b, Supplementary Fig. 16b). Complementally, the levels of major oxidative products were also elevated as presented in Fig. 7c–e, indicating that oxidative stress occurred in these two groups after US stimulation.

Immunofluorescence was used to confirm overexpression of UCP1 in adipose tissue of mice after treatment with the CRISPRa system. In contrast to the control group, the expression of *UCP1* was increased in the IgWAT of mice in the MN-aUCP1, MN-MP/aUCP1, MN-MP + US and MN-MP/aUCP1 + US groups (Fig. 7f, Supplementary Fig. 16c), which was also confirmed by equivalent detections of mRNA and protein levels (Fig. 7g, h). Meanwhile, the results from real-time PCR and western blot analysis revealed a significant increase in the expression level of *PGC1-β* and a decrease in the expression level of *PPARγ* in IgWAT of the MN-MP/aUCP1 + US group (Fig. 7h–j). *PGC1-β* is recognized as a critical regulator of mitochondrial metabolism, while *PPARγ* acts as an indicator of adipogenesis, promoting adipogenesis and lipid synthesis[34,35]. It is noteworthy that these gene expression changes were not only significant in the MN-aUCP1 and MN-MP/aUCP1group but also in the MN-MP + US group, demonstrating that both CRISPRa-UCP1 and sonodynamic effect jointly to these outcomes (Fig. 7g–j). Additionally, PPARα, predominantly found in brown/beige adipocytes, was also upregulated in IgWAT of the MN-MP/aUCP1 + US group (Supplementary Fig. 16d). Consistent with expectations, the sono-gene treatment significantly lowered adipose TG content and raised FFA levels (Fig. 7k and Supplementary Fig. 16e). The results of Sanger sequencing showed that the sono-gene editing system only resulted in stable overexpression of the target gene, without gene mutation (Supplementary Fig. 17a). Taken together, these findings further supported the idea that MN-MP/aUCP1 + US maximized counterbalancing obesity by triggering excessive white adipocytes apoptosis and enhancing metabolism.

To further investigate the potential correlation between MN-MP/aUCP1 + US treatment and the observed enhancement in metabolic function, we assessed whether the increased energy expenditure in mice was attributable to AMP-activated protein kinase (AMPK) activation. The enzyme activity of AMPK serves as a crucial mediator of metabolic flux across various tissues in response to heightened energy demand[36]. The activation of AMPK necessitates the phosphorylation of threonine 172 within the AMPK catalytic subunit by an upstream kinase[36]. We observed that, compared to the control group, the MN-aUCP1 and MN-MP/aUCP1 groups exhibited a significant decrease in ATP levels in IgWAT, which corresponded with increased AMP levels and elevated [AMP] to [ATP] ratio (Supplementary Fig. 17b–d). Additionally, phospho-AMPKα (Thr172) (p-AMPK) protein levels were elevated in MN-MP/aUCP1 + US group (Fig. 7l). When comparing MN + US with MN-MP + US-treated mice, we observed that the latter exhibited significantly higher p-AMPK levels in IgWAT benefiting from sonodynamic effect (Fig. 7l). To determine whether sustained overexpression of UCP1 relies on AMPK activation, mature adipocytes were treated with CRISPRa-UCP1 and the AMPK inhibitor (compound C, CC). We found that the presence of the AMPK inhibitor not only inhibited AMPK activation (Fig. 7m) but also impaired UCP1 expression (Fig. 7n). Consistently, CC mitigated the inhibition of TG content by aUCP1 (Supplementary Fig. 17e). Additionally, *PGC1-β* levels were reduced by the inhibition of AMPK activation (Supplementary Fig. 17f). Taken together, these data suggested that MN-MP/aUCP1 + US treatment enhanced metabolic function by synergistically activating AMPK through sonodynamic effect and UCP1 overexpression.

Mechanistic exploration of the weight-loss capacity of MN-MP/aUCP1 + US

As stated above, the molecular level of IgWAT from mice exhibited dramatic alterations after treatment with the US-stimulated CRISPRa-UCP1 system. To investigate the mechanisms behind these alterations, we performed transcriptome sequencing analysis of IgWAT in untreated obese mice and MN-MP/aUCP1 + US-treated mice to determine their transcriptional profiles. The results of the principal component analysis indicated clear clustering of the control and treatment samples, revealing distinct gene expression profiles (Supplementary Fig. 17g). A total of 5791 differentially expressed genes (DEGs) profiles were identified through screening based on the criteria of a p-value < 0.05 and a fold change >2.0, including 2896 up-regulated genes and 2895 down-regulated genes (Fig. 8a–c). The gene ontology (GO) analysis displayed that DEGs were significantly enriched in the biological

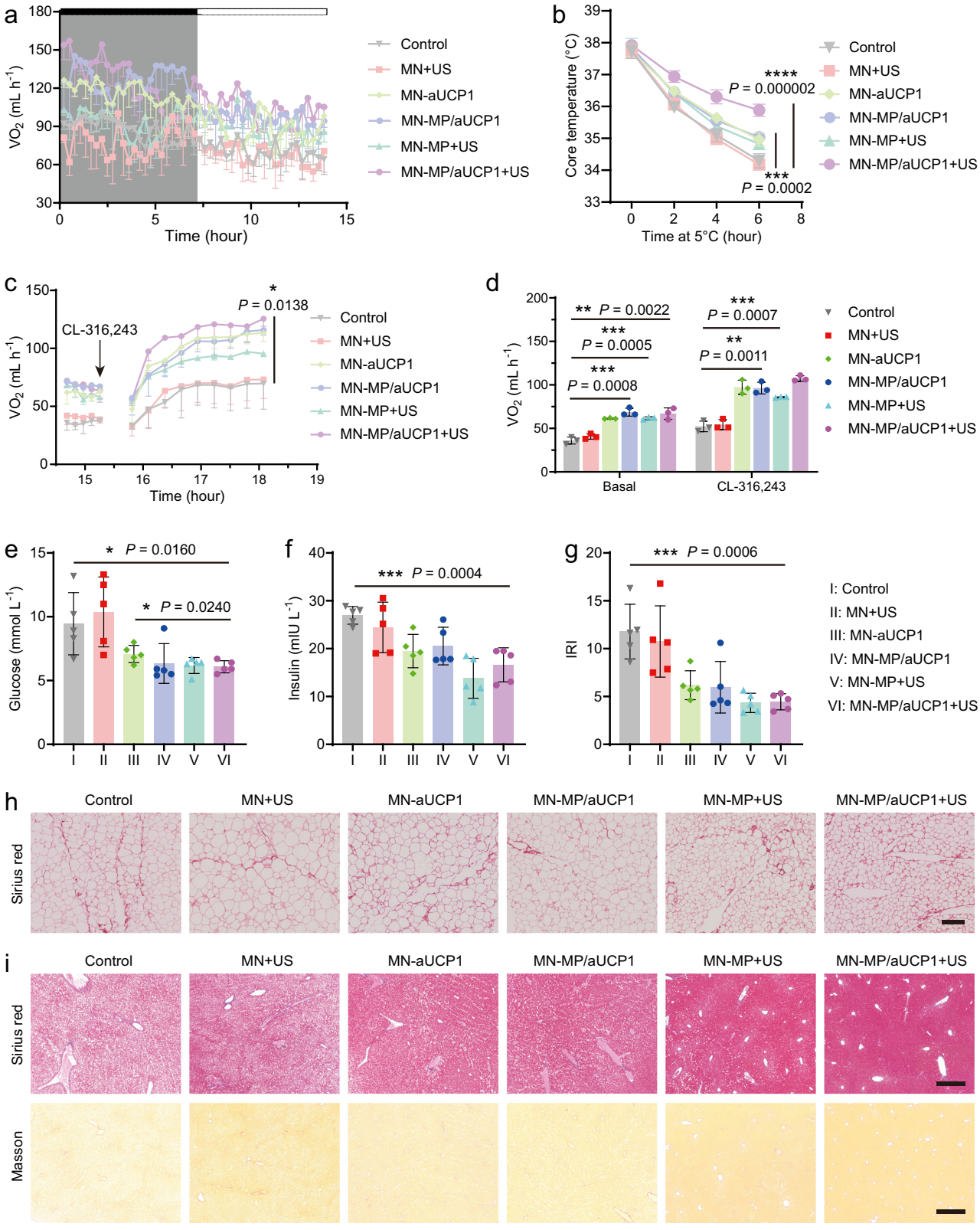

process (BP) of lipid alteration and browning-related functions, mainly including lipid metabolic process, fatty acid metabolic process, brown adipocyte differentiation and fatty acid β-oxidation (Fig. 8d). The DEGs were found to be enriched in cellular components such as mitochondria and peroxisomes, among others. Also, they were annotated as being involved in receptor binding, including lipid and ATP binding (Fig. 8d). Gene set enrichment analysis (GSEA) unmasked increased expression of genes involved in the positive regulation of ROS metabolic process and regulation of apoptotic process in isolated IgWAT after MN-MP/aUCP1 + US treatment, which proved that US-augmented genome editing treatment effectively enhanced ROS production and induced apoptosis of adipocytes (Fig. 8e). On the flip side, it has been confirmed that *UCP1* overexpression can alter fat formation and lipid homeostasis by reducing de novo lipogenesis in IgWAT through the

Fig. 6 | Improvement of metabolic dysfunction related to obesity in mice after treatment with MN-MP/aUCP1 + US. a Oxygen consumption (VO_2) of mice over a 14 h dark/light cycle (shown as the gray/white background of the chart) on day 19 after various treatments. Data are presented as means ± SD ($n = 3$ mice per group). **b** The body core temperature change over time in different treated mice at 5 °C. Data are presented as means ± SD ($n = 5$ mice per group). CL-316,243-stimulated VO_2 (**c**) at different time and corresponding average VO_2 (**d**) of different treated mice housed at thermoneutrality (30 °C). Data are presented as means ± SD ($n = 3$ mice per group). Serum glucose (**e**) and insulin (**f**) levels of mice on day 21 after various treatments. IRI (**g**) calculated from the above serum glucose and insulin levels. Data are presented as means ± SD ($n = 5$ biologically independent samples). **h** Sirius red staining of IgWAT from mice in different groups after 21 days of treatment (Scale bar: 100 μm). **i** Sirius red staining and masson staining of livers from mice in different groups after 21 days of treatment (Scale bars: 500 μm). The experiments for **h** and **i** were repeated three times independently with similar results. Statistical differences for **b**–**g** were calculated using two-tailed unpaired student's *t*-test. $^*P < 0.05$, $^{**}P < 0.01$, $^{***}P < 0.001$, and $^{****}P < 0.0001$. Source data are provided as a Source Data file.

inhibition of transcription activation of lipogenic gene programs[37,38]. Adipocytes from control mice showed enrichment for the gene ontology terms "lipid homeostasis" and "lipid droplet organisation", whereas those from treated mice did not, suggesting that CRISPRa-UCP1 system with US therapy exerted promising therapeutic potential (Fig. 8f). More importantly, the heatmap of DEGs uncovered upregulation of genes involved glucose or fatty acid metabolism, as well as clear increases in the expressions of mitochondria-related gene. These data together further indicated that metabolic processes and mitochondrial function were elevated in IgWAT of MN-MP/aUCP1 + US-treated mice. In contrast, lipogenesis and differentiation-related genes (*Fabp4*, *Pparg*, etc.) were significantly suppressed (Fig. 8g). Collectively, our study demonstrated a sono-gene therapy platform that could be controlled temporally and spatially to improve obesity and insulin resistance by enhancing systematic metabolic processes, and effectively restrict weight regain.

Discussion

Obesity is a worldwide issue, with approximately 2.8 million deaths annually attributed to obesity and related complications[39,40]. Without intervention, it is projected that over half of the global population will be overweight by 2035[39]. Therefore, the increasing prevalence of obesity necessitates a multifaceted approach to prevention and treatment[41]. Recent research has confirmed that obesity is a chronic and complex disease that requires intensive lifestyle interventions, effective pharmacological treatments, and endoscopic and surgical approaches[42,43]. Among them, the emergence of glucagon-like peptide 1 (GLP1) receptor agonists has shown promising results[44]. Despite the availability of various treatments, there are limitations such as severe gastrointestinal side effects, suboptimal weight loss outcomes, weight regain post-treatment cessation, and serious complications following bariatric surgery[43,44]. Hence, it remains imperative to develop strategies to ensure equitable access to long-term effective anti-obesity treatment outcomes. Here, we have developed an intelligent and effective US-induced gene regulation strategy to treat obesity, with a temporally and spatially controlled US stimulation, inducing adipocyte apoptosis and browning.

This spatiotemporal responsive SDT combined with genome editing therapy has unique advantages. First of all, compared with the existing photodynamic and photothermal therapy strategies, SDT has a higher penetration ability. The US-controlled MN patch can be inserted into the subcutaneous fat layer at the corresponding position of the viscera according to the treatment needs. This can reduce visceral fat and alleviate visceral diseases caused by fat burden, making it possible for individuals with obesity to target specific areas for weight loss. In addition, SDT, on one hand, stimulated the expression of thermogenesis-related genes, and on the other hand, promoted the controlled release of the MP/aUCP1 system from MN patches, thereby playing a synergistic role in the browning of white adipocytes to enhance thermogenesis and metabolism in mice. Furthermore, SDT can induce ROS production to facilitate the apoptosis of excess white adipocytes. It is noteworthy that elevated ROS levels in adipocytes can also drive elevated adipocyte thermogenesis, which is highly beneficial in fat loss[11,45,46]. Excitingly, the progression of UCP1-dependent thermogenesis can be supported by elevated ROS levels[45]. Thereby, a good effect for anti-obesity is foreseeable using US-triggered CRISPRa-UCP1 system.

On the other hand, cryolipolysis, a popular fat reduction method, works by triggering apoptosis. While generally deemed a safe and non-invasive treatment, there have been reports in recent years of serious and long-term side effects, including paradoxical fat hyperplasia and fibrosis[47,48]. Fortunately, our treatment regimen did not exacerbate fibrosis in the liver or adipose tissue when compared to the control group.

Notably, this study offered mechanistic insights into the innovative sono-gene therapy platform. The observed reductions in serum TG and cholesterol and metabolic cage studies provided compelling evidence that sono-gene therapy-mediated changes in adipose tissue transcriptome profiles could subsequently influence systemic metabolism. Furthermore, our data indicated that adipogenesis and differentiation were diminished in treated IgWAT. Studies have shown that adipose-tissue insufficiency (as in lipoatrophy) induced by adipocyte differentiation disorders leads to high circulating glucose and cholesterol levels, which is a hallmark of and contributor to insulin resistance[49,50]. Encouragingly, our sono-gene therapy platform not only significantly avoided the risks associated with lipoatrophy but also led to marked improvements in insulin resistance. Moreover, the oxidative stress caused by ROS did not lead to systemic inflammation, possibly benefit from the anti-inflammatory properties of HA[51].

Of clinical significance, this study can be regarded as an attractive therapeutic approach, promising to maximize clinical outcomes against obesity and other metabolic diseases at spatiotemporally controllable sono-gene therapy platform.

Methods

Ethical issues

All mouse experiments for the whole study were performed according to protocols in accordance with the policies of the National Ministry of Health and approved by the Laboratory Animal Center of Shanghai Tenth People's Hospital (SHDSYY-2022-272701).

Materials

All chemicals in our study were obtained from Sigma-Aldrich unless otherwise specified. Tetrakis (4-carboxyphenyl) porphyrin (TCPP, 97%) was purchased from Tokyo Chemical Industry Co., Ltd. Ethanol was acquired from Merck. Pyrazine (99%) was purchased from Aladdin. SDS-PAGE Gel Rapid Preparation Kit was obtained from Beyotime Co. Ltd. Hyaluronic acid (10 kDa) was purchased from Meilun Biotechnology Co., Ltd. Dulbecco's Modified Eagle Medium (DMEM), calf serum, and fetal bovine serum (FBS) were acquired from Biological Industries. Annexin V-FITC apoptosis detection kit, CCK-8, Calcein/PI cell viability/cytotoxicity, ROS and TUNEL assay kits were purchased from Beyotime Biotechnology. Mouse IL-6, IL-1β and TNF-α ELISA Kits were purchased from YOBIBIO (Shanghai, China). Glucose and insulin assay kits, FFA, TG, MDA, cortisol and NE assay kits, and 4-HNE and 8-OHdG ELISA Kits were purchased from Nanjing Jiancheng Bioengineering Institute. AMP and ATP measurement kits were obtained from Jiwei Biological Technology (Shanghai, China). The anti-β-actin antibody, anti-PGC1-β antibody, anti-PPARα antibody and anti-PPARγ antibody were gained from Abcam. The anti-UCP1 antibody, anti-

https://doi.org/10.1038/s41467-025-56755-4

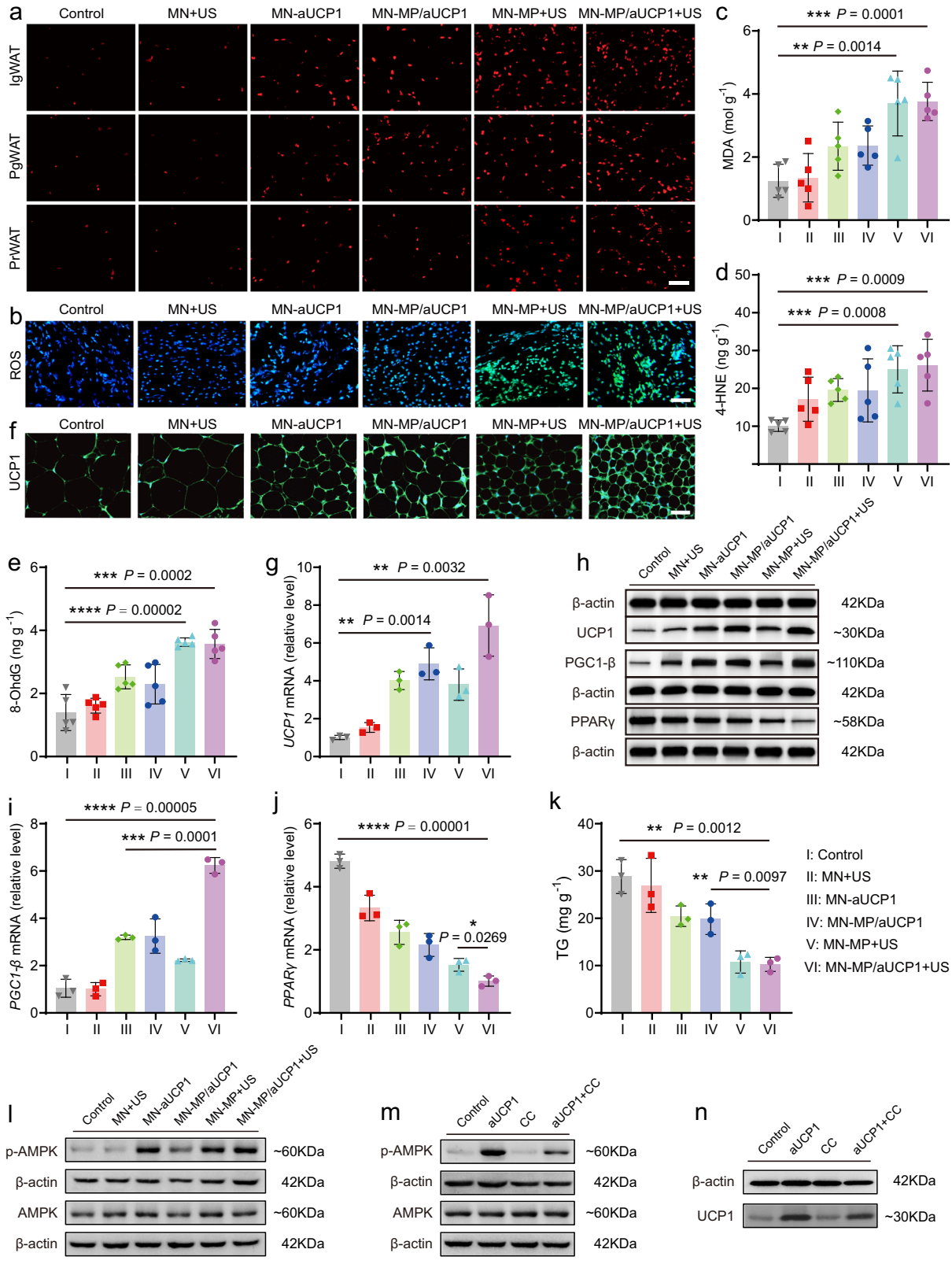

phospho-AMPKα (Thr172) antibody and anti-AMPKα antibody were gained from Cell Signaling.

Characterizations

The morphology of MOF (Zn-TCPP) and MP/aUCP1 nanosheets was obtained by TEM (FEI Tecnai G2 F20, accelerating voltage = 200 kV). Corresponding elemental mappings were observed by JEM-2100F. XPS was performed by x-ray photoelectron spectrometer (Thermo escalab 250XI). UV-vis absorbance spectrum was examined by UV-vis-NIR spectrophotometer (PE Lambda 950). FT-IR was investigated by Shimadzu IR Prestige-21 FT-IR spectrometer. Size and zeta potential were detected by Malvern Zeta Particle Sizer Nano Series (Nano ZS90). XRD patterns were tested with a bruker D8 X-ray diffractometer. The confocal images were captured by a CLSM (Carl Zeiss, LSM 900). $^1O_2$

Fig. 7 | Alterations at the molecular level of IgWAT after MN-MP/aUCP1 + US treatment. a Representative TUNEL images presenting apoptosis (red) in IgWAT, PgWAT and PrWAT (Scale bar: 50 μm). **b** Representative fluorescence images of ROS levels (green) and nuclei stained with DAPI (blue) within IgWAT (Scale bar: 50 μm). **c**–**e** Oxidative stress levels within IgWAT of different treatment groups, including MDA (c), 4-HNE (d) and 8-OHdG (e). Data are presented as means ± SD ($n = 5$ biologically independent samples). **f** Representative UCP1-labelled immunofluorescence (green) images of IgWAT slices (Scale bar: 50 μm). **g** mRNA expressions of *UCP1* within IgWAT in different groups of mice. Data are presented as means ± SD ($n = 3$ biologically independent samples). **h** Western blots of UCP1, PGC1-β and PPARγ in IgWAT. **i, j** mRNA expressions of *PGC1-β* (i) and *PPARγ* (j). Data are presented as means ± SD ($n = 3$ biologically independent samples). **k** Determination of TG content in IgWAT. Data are presented as means ± SD ($n = 3$ biologically independent samples). **l** Western blot of p-AMPK and AMPK in IgWAT. Protein levels of p-AMPK, AMPK (**m**) and UCP1 (**n**) in mature adipocytes after different treatments. The experiments for **a**, **b**, **f**, **h**, **l**, **m**, and **n** were repeated three times independently with similar results. Statistical differences for **c**–**e, g**, and **i**–**k** were calculated using two-tailed unpaired student's *t*-test. $^{*}P < 0.05$, $^{**}P < 0.01$, $^{***}P < 0.001$, and $^{****}P < 0.0001$. Source data are provided as a Source Data file.

detection was identified by the electron spin resonance (ESR) spectrometer (200A300-10/12). The morphology of MN patch was observed by SEM (ZEISS GeminiSEM 300). Fluorescent sections were observed with Nikon bio-microscope (CI-L).

Synthesis of MOF (Zn-TCPP) nanosheets

PVP (100 mg), $Zn(NO_3)_2{\cdot}6H_2O$ (22.5 mg, 0.075 mmol) and pyrazine (4 mg, 0.05 mmol) were dissolved in 60 mL of a mixture of DMF and ethanol (V:V = 3:1) in an 80 mL brown flask with a cap. TCPP (20 mg, 0.025 mmol) dissolved in 20 mL of the mixture of DMF and ethanol (V:V = 3:1) were then added drop wisely under stirring. Next, the prepared solution was sonicated for 20 minutes. The vial was placed in a water bath with magnetic stirring pot to react at 80 °C for 16 h. MOF (Zn-TCPP) nanosheets were obtained after washing twice with ethanol and centrifuging at 7100 × *g* for 8 min. Subsequently, the collected Zn-TCPP nanosheets were dispersed in 50 mL of ethanol. UV-Vis: λmax 435 nm; IR: 1600 cm^{-1}, 1400 cm^{-1}, 995 cm^{-1}.

Construction of CRISPRa-UCP1

The target of *UCP1* gene sequence (AGGGCTTTGGGAGTGACGCG) was designed using the online tool: [http://chopchop.cbu.uib.no/]. SP-dCas9-VPR and PX330 (from Addgene) were used as vectors. CRISPRa was cloned according to Gibson assembly guide lines. Supplementary Table 1 contains sequences of the plasmid encoding pEGFP.

Cell culture

The 3T3-L1 embryonic fibroblasts (Catalog No. CL-173) were purchased from the American Type Culture Collection (ATCC, Manassas, VA, US) and were cultured in DMEM medium that containing 10% calf serum at 37 °C with 5% CO_2. The cell line was quarterly authenticated and ensured to be no mycoplasma contamination. For the differentiation of 3T3-L1 preadipocytes, when cell fusion reached 100%, configured MDI induction medium (90% DMEM, 10% FBS, 0.5 mM 3-isobutyl-1-methylxanthine, 1 μM dexamethasone, and 10 μg mL^{-1} insulin) were added and cultured for 2 days, and then switched to DMEM containing 10% FBS and 1 μM dexamethasone) for 2 days. Subsequently, the culture medium changed to DMEM medium containing 10% FBS for continued maintenance, with fluid changes every 2 days, until 3T3-L1 preadipocytes were induced into mature adipocytes on day 8–10.

Western blotting of mature adipocytes

Following differentiation of 3T3-L1 preadipocytes into mature adipocytes, the CRISPRa-UCP1 plasmid (10 μg mL^{-1}, complexed with Lipofectamine 2000) was treated on mature adipocytes for 3 days. Total protein concentration was assessed using a BCA protein assay kit. An equal amount of protein (25 μg) was separated in 12% sodium dodecyl sulfate polyacrylamide gel. The proteins were transferred to PVDF membranes and subjected to incubation with blocking buffers at room temperature for 1 h. The membrane was incubated with a 1000-fold dilution of anti-UCP1 antibody (Cell Signaling, Catalog No. 72298) and anti-β-actin antibody (Abcam, Catalog No. ab8227) overnight, followed by immersion in the coupled secondary antibody at room temperature for 1 h. Western Lightning Chemiluminescence Reagent Plus (PerkinElmer) was used for visualization. Images were acquired with the Automatic Chemiluminescence Imaging System (Tanon 5200) and analyzed with ImageLab software (Bio-Rad). The uncropped scans of the blots are supplied as Source Data files.

Synthesis of P/aUCP1, MP and MP/aUCP1 nanosheets

The mixture of mPEG and PEI (w: w = 1: 2) and aUCP1 were mixed and stirred overnight at a mass ratio of 1: 1.25 to prepare P/aUCP1. 40 mg of Zn-TCPP was dispersed in 5 mL of PBS, to which 10 mg of a mixture of mPEG and PEI (w: w = 1: 2) was added, and stirred overnight at room temperature in the dark. Then the mPEG-PEI modified Zn-TCPP (MP) was obtained. MP/aUCP1 nanosheets were obtained by mixing MP with aUCP1 for 2 h at a mass ratio of 4: 1.

Agarose gel electrophoresis assay

CRISPRa-UCP1 plasmid with varying mass ratios were combined and incubated with MP overnight. The mixture was then centrifuged at 7100 × *g* for 8 min to collect the supernatant. Subsequently, 5 μL of supernatant with different mass ratios was mixed with 1 μL of 6× DNA loading buffer to prepare various loading solutions. These loading solutions were then applied to sample wells within a 0.5% agarose gel, followed by electrophoresis at 80 V for 40 min. Gel imaging was performed using a gel recording system (ChampChemi 910 Plus). The uncropped scan of the gel is supplied as Source Data files.

Evaluation of sonodynamic property in vitro

The ability of MP/aUCP1 to produce $^1O_2$ in vitro was evaluated using DPBF as an indicator of $^1O_2$, under US irradiation. To test this, the DMSO solution containing DPBF (5 μL, 10 mM) was mixed with 50 μg mL^{-1} of MP/aUCP1 solution. The UV-vis absorption spectra of DPBF were determined to evaluate the production of $^1O_2$ after different durations of irradiation (0 min,1 min, 2 min, 3 min, and 4 min) with US (1.0 MHz, 1.5 W cm^{-2}, 50% duty cycle). Additionally, TEMP was used as the trapping agent to detect $^1O_2$ by ESR spectrometer in different treatment groups, including H_2O + TEMP + US irradiation (1.0 MHz, 1.5 W cm^{-2}, 50% duty cycle, 5 min), TEMP + MP/aUCP1(50 μg mL^{-1}), and MP/aUCP1 (50 μg mL^{-1}) + TEMP + US irradiation (1.0 MHz, 1.5 W cm^{-2}, 50% duty cycle, 5 min).

Sonodynamic property and anti-obesity performance at the cellular level

To validate sonodynamic property at the cellular level, the preadipocytes and mature adipocytes were divided into six groups: (I) control, (II) US irradiation, (III) aUCP1 (10 μg mL^{-1} complexed with Lipofectamine 2000 according to the manufacturer's instructions), (IV) MP/aUCP1 (50 μg mL^{-1}), (V) MP (40 μg mL^{-1}) + US irradiation and (VI) MP/aUCP1 (50 μg mL^{-1}) + US irradiation. Cells were incubated with various samples for 12 h. Then, US irradiation (1.0 MHz, 1.5 W cm^{-2}, 50% duty cycle, 5 min) was performed on groups (II), (V), and (VI). To evaluate the cellular apoptosis, the mature adipocytes were stained with Annexin V-FITC and PI solution for 30 minutes, followed by FCM analysis (FACS Aria II, BD Biosciences). Data collection was used with a multi-application cell sorter (Sony Biotechnology, MA900). For Calcein-AM/PI staining assay, the preadipocytes were stained with Calcein-AM and PI solution for 30 minutes, followed by fluorescence

https://doi.org/10.1038/s41467-025-56755-4

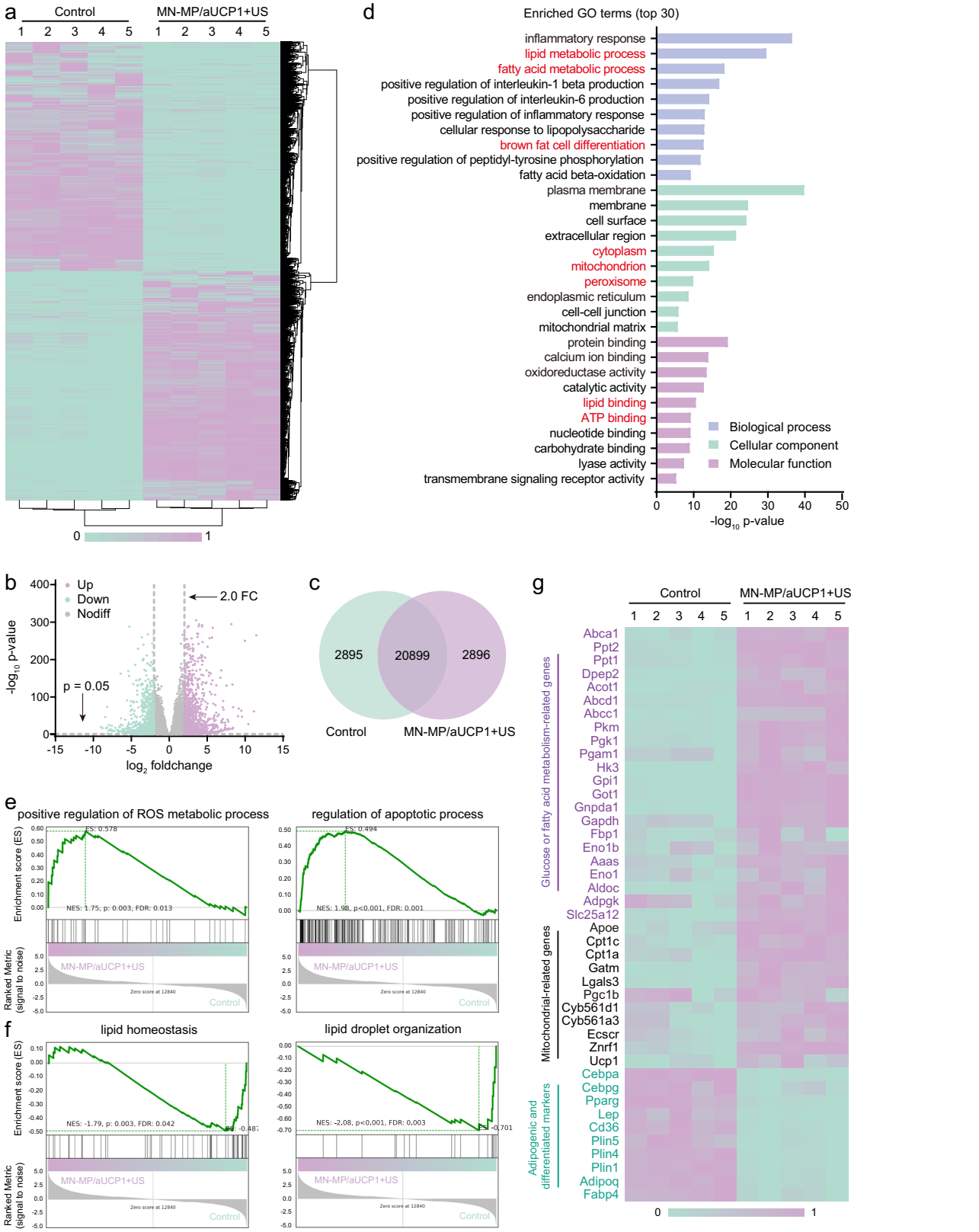

Fig. 8 | Mechanistic exploration of the weight-loss capacity of MN-MP/aUCP1 + US. Cluster analysis (**a**), volcano map (**b**) and venn diagram (**c**) of DEGs in RNAseq between untreated and MN-MP/aUCP1 + US treated IgWAT 21 days post treatment ($n = 5$ biologically independent samples). ($P < 0.05$, |fold change| ≥2). Statistical difference was calculated using Negative binomial distribution test. **d** Significant enrichment in GO terms (top 30, $n = 5$ biologically independent samples). **e, f** GSEA on RNAseq data of IgWAT isolated from untreated and MN-MP/aUCP1 + US treated mice ($n = 5$ biologically independent samples). **g** Heatmap of DEGs associated with glucose or fatty acid metabolism, mitochondria, and lipogenesis and differentiation ($n = 5$ biologically independent samples). Statistical differences for **d, e**, and **f** were calculated using Fisher's exact test.

microscope observation. ROS production of mature adipocytes was observed using CLSM and FCM analysis 1 h after loading with the DCFH-DA probe.

Intracellular TG content was quantified by colorimetric assay kit. The mature adipocytes were divided into six groups as above. Cells were incubated with various samples for 12 hours. Then, US irradiation (1.0 MHz, 1.5 W cm^{-2}, 50% duty cycle, 5 min) was performed on groups (II), (V), and (VI). After 24 hours, Intracellular TG levels were measured according to the manufacturer's instructions.

The cell viability of 3T3-L1 preadipocytes and mature adipocytes was evaluated via standard CCK-8 assay. 3T3-L1 preadipocytes and mature adipocytes were inoculated in 96-well plates (10^4 per well) and cultured overnight. Then, various treatments were conducted including incubation with different concentrations of MP/aUCP1 nanosystems (0, 2.5, 5, 10, 25, and 50 μg mL^{-1}) and incubation with MP/aUCP1 (50 μg mL^{-1}) + irradiation by US with various power densities (0, 0.25, 0.5, 0.75, 1, and 1.5 W cm^{-2}; 1.0 MHz, 50% duty cycle, 5 min) for 24 h. The cells were washed three times with PBS. Then, 10% CCK-8 solution was added for another 1 hour. The absorbance at 450 nm was measured with a microplate reader (Bio-TekELx800, USA) to evaluate the cell viability.

Analyses of cellular uptake and lysosomal escape

P/aUCP1-FITC, aUCP1-FITC, and MP/aUCP1-FITC were generated through FITC modification of P/aUCP1, aUCP1(complexed with Lipofectamine 2000), and MP/aUCP1. The induced differentiated mature adipocytes were divided into four groups: P/aUCP1-FITC (18 μg mL^{-1}), aUCP1-FITC (10 μg mL^{-1}), MP/aUCP1-FITC (50 μg mL^{-1}), and MP/aUCP1-FITC + US (MP/aUCP1, 50 μg mL^{-1}; US, 1.0 MHz, 1.5 W cm^{-2}, 50% duty cycle, 5 min). After four hours, the cell nuclei were stained with DAPI, washed three times with PBS, and fixed with 4% paraformaldehyde. The uptake of the material was observed using CLSM. To analyze lysosomal escape, lysosomes/endosomes and nuclei were stained with Lyso-Tracker Red and DAPI four hours after cell treatment. Subsequently, the cells were washed three times with PBS, fixed with 4% paraformaldehyde, and observed under CLSM.

Evaluation of gene transfection ability

The preadipocytes and mature adipocytes were divided into four groups: PBS, P/aUCP1@EGFP (18 μg mL^{-1}), aUCP1@EGFP (10 μg mL^{-1}), MP/aUCP1@EGFP (50 μg mL^{-1}), and MP/aUCP1@EGFP + US (MP/aUCP1, 50 μg mL^{-1}; US, 1.0 MHz, 1.5 W cm^{-2}, 50% duty cycle, 5 min). The cells were then cultured for 6 h before being replenished with fresh DMEM culture medium and co-cultured for an additional day. Subsequently, the transfection efficiency of the harvested cells was assessed using FCM and fluorescence microscope.

Preparation of microneedle (MN) patch

The MN patch was created using a polydimethylsiloxane (PDMS) mold with each needle cavity having a 300 μm-by-300 μm quadrate substrate tapering to a height of 800 μm. The MNs were arranged in a 12-by-12 array with a center-separated 600 μm. To prepare the MN patch, HA solution was prepared by solubilize 15 wt % HA in PBS. 100 μL HA solution mixed with MP (80 μg), aUCP1 (20 μg complexed with Lipofectamine 2000), and MP/aUCP1 (100 μg) was deposited in the needle cavities, respectively, and dried under vacuum for 20 min. The needle chambers were then filled with 100 μL of HA solution, and the micromold was kept at 25 °C overnight to form the MN patch. SEM was used to observe the morphology of empty and drug-loaded MNs. 10 wt%, 15 wt% or 20 wt% HA MN patches were prepared, and the mechanical strength of the MNs was measured using a tensile testing machine (WDW-10).

Mice

Given that male obese mice often show higher susceptibility to obesity, this study utilized male mice to establish an obesity model induced by high-fat diets. Male C57BL/6 J mice aged 6–8 weeks were purchased from Ling Chang Biological Technology Co., Ltd. Mice were housed under controlled conditions of temperature (22 °C) and illumination (12 h light cycle, with lights on at 07:00), maintaining a humidity level of approximately 50%. The mice were fed HFD (Wuxi Fanbo Biotechnology Co., Ltd., FB-D12492, 60% fat) for about 8 weeks, increasing body weight from ≈18 g to ≈35 g. Water was provided ad libitum.

Characterization of MN-MP/aUCP1 patch

MN patches containing varying amounts of MP/aUCP1 were fabricated and subjected to mechanical strength testing. To assess the transfection efficiency of drug-loaded MN patches post-US irradiation, different MNs were incubated with mature adipose tissue for 6 h, followed by replacement with fresh DMEM culture medium and an additional day of culture. Subsequently, the collected cells were evaluated for transfection efficacy using FCM. aUCP1-ICG and MP/Cy3 were used to prepare MN patches for fluorescence imaging. The aUCP1 solution was mixed with ICG, stirred at room temperature in the dark for 24 h, and aUCP1 labeled with ICG was obtained after dialysis. MP/Cy3 was obtained by stirring MP with Cy3 in the dark for 24 hours and then centrifugation. The fluorescence images of MN patches were taken by CLSM.

The biological distribution of aUCP1 and MP/aUCP1 was monitored by in vivo imaging system (IVIS) spectrum imaging system (VISQUE Invivo Smart-LF) after subcutaneous injection and MN patch administration in the inguinal region. aUCP1 loaded with ICG was prepared according to the above-described process. The aUCP1 or MP/aUCP1 loaded with ICG was injected directly into the IgWAT region of obese mice by in situ injection and MN patch. The dosage of ICG fluorescent dye was the same in all groups. The biological distribution of ICG in mice at day 0, day 1, day 2, and day 3 after dosing was observed by IVIS spectrum imaging system ($n = 3$ mice per group). In addition, on days 1, 2, and 3 after administration, mice were euthanized by carbon dioxide followed by cervical dislocation, separating the major organs (heart, liver, spleen, lung, kidney) and IgWAT. The biological distribution of ICG in major organs and IgWAT of mice was observed ($n = 3$ mice per group).

In vivo obesity treatment with MN-MP/aUCP1 patch

The diet-induced obese mice were divided randomly into six groups, including control, MN + US irradiation, MN-aUCP1, MN-MP/aUCP1, MN-MP + US irradiation, and MN-MP/aUCP1 + US irradiation ($n = 5$ per group). The mice were shaved the abdominal hair and anesthetized, and different drug-loaded MN patches were inserted into the subcutaneous fat layer of the right inguinal region. After 15 min, the MN-inserted abdomen of mouse was irradiated used a 1 cm^2 ultrasonic probe at 1.0 MHz, 1.5 W cm^{-2}, 50% duty cycle for 5 min. Each mouse received 7 courses of treatment, for one time every 3 days. During the treatments, food intake and body weight of mice were monitored every 3 days. The skin temperature in the BAT region were recorded with an infrared thermal imaging camera (Magnity Electronics).

At the end of 21 days of treatment, blood samples were taken from mice fasted for 12 h by retro-orbital puncture and centrifuged for serum. The levels of serum glucose and insulin were measured by assay kits to calculate IRI as the serum glucose (mmol L^{-1}) × serum insulin (mIU L^{-1})/22.5. Subsequently, the mice were subjected to an oral glucose tolerance test. Mice were given glucose (2 g kg^{-1}) by oral gavage. Glucose concentration in blood from the tail vein was measured by glucose meter (Yuwell) at 0, 0.5, and 2 h. Then, mice were sacrificed, blood samples were obtained for routine blood analysis and serum biochemical assays. The serum levels of FFA, IL-6, IL-1β and TNF-α were measured with corresponding kits according to the manufacturer's instructions. The major organs (heart, liver, spleen, lung and kidney) were collected for H&E staining.

Meanwhile, the liver fibrosis was observed by Sirius red staining and Masson staining. Fresh livers were prepared into frozen sections

and stained with oil red O to characterize the extent of lipid droplet infiltration. Inguinal, perigonadal, perirenal adipose tissues were isolated from each mouse, fixed, wrapped in paraffin, and cut into sections. The size of adipose tissue was observed by H&E staining. TUNEL assay kit was used to detect apoptotic cells in adipose tissue of different parts. Immunofluorescence staining of IgWAT was performed with anti-UCP1 Antibody (1:100 dilution). The IgWAT fibrosis was observed by Sirius red staining. Fresh IgWATs were prepared into frozen slices to detect ROS levels. MDA content was detected by colorimetric kit. Determinations of 4-HNE, 8-OHdG, TG, AMP, and ATP levels were used by corresponding kits.

Total RNA was extracted from IgWATs using TRIzol reagent (Invitrogen) and synthesized cDNA using the reverse transcription system (Thermo Fisher). Primer sequences specific for *UCP1*, *PGC1-β* and *PPARγ* were used (Supplementary Table 2), and the relative gene expression was assessed by a 7500 real-time PCR system (ABI Step one plus, Applied Biosystems). Additionally, UCP1, PGC1-β, PPARγ, PPARα p-AMPK and AMPK levels were assessed by western blotting with anti-UCP1 antibody (Cell Signaling, Catalog No. 72298), anti-PGC1-β antibody (Abcam, Catalog No. ab176328), anti-PPARγ antibody (Abcam, Catalog No. ab178860), anti-PPARα antibody (Abcam, Catalog No. ab314112), anti-phospho-AMPKα (Thr172) antibody (Cell Signaling, Catalog No. 2531), and anti-AMPKα antibody (Cell Signaling, Catalog No. 2532) (1:1000 dilution), respectively. The uncropped scans of the blots are supplied as Source Data files. Sanger sequencing was performed using a 3730xl sequencer (Applied Biosystems), and the sequencing results were interpreted by Sequencing Analysis 5.2.0 software.

Monitor of weight regain post MN-MP/aUCP1 + US treatment

After 21 days of treatment with MN-MP/aUCP1 + US, period mice were monitored for HFD and weight regain for further 15 days ($n = 3$ mice per group). The food intake of mice was recorded daily, and the weight was measured at day 24, day 30 and day 36 during this period.

Metabolic physio-cage studies

A cohort of obese mouse models was constructed to specialize in metabolic studies ($n = 3$ mice per group). On day 19 following seven courses of treatment, mice were housed within metabolic physio-cages of a Comprehensive Lab Animal Monitoring System (CLAMS). Prior to formal testing, all the mice were acclimated to the system for 12 h, during which they had free access to food and water. After the metabolic monitoring, the mice received an intraperitoneal injection of 1 mg kg^{-1} of the β3-adrenergic receptor-specific agonist CL-316,243. The metabolic cages were utilized again to observe the mice's responses to adrenergic stimulation. During the monitoring period, VO_2, heat production, and cumulative food intake were collected. Additionally, activity level was also measured using an OPTO-M3 sensor system.

In studies involving acute administration, obese mouse models were established and the mice were monitored in the metabolic cages after three consecutive days of treatment ($n = 3$ mice per group). The monitoring indicators are the same as above. Mice were then sacrificed, serum samples and IgWAT were obtained to measure NE and cortisol levels using the corresponding assay kits.

Cold exposure test

Mice were subjected to a temperature of 5°C to evaluate their cold endurance ($n = 5$ per group). Rectal temperatures were recorded at 0, 2, 4, and 6 h using a digital thermometer (TH-212, China) to assess core body temperature. The mice were provided with unrestricted access to water throughout the experiment.

In vitro inhibitors treatment

To investigate whether sustained overexpression of UCP1 relied on AMPK activation, mature adipocytes were treated with aUCP1 (10 μg mL^{-1}, complexed with Lipofectamine 2000) and/or the inhibitor CC (10 μM). After 48 h, western blotting was used to analyze the protein expression of AMPK, p-AMPK and UCP1 in different treated cells. The intracellular TG content and *PGC1-β* mRNA level were detected according to the above methods.

RNA-sequencing

IgWATs were isolated from mice after 7 courses of treatment with MN-MP/aUCP1 + US, and IgWATs from obese mice were taken as a control ($n = 5$ per group). RNA of IgWAT was extracted using HiPure Universal RNA Mini Kit (Magen Biotechnology Co. Ltd). RNA sequencing was performed using RNA Nano 6000 Assay Kit of the Agilent Bioanalyzer 2100 system (Agilent Technologies).

Statistical analysis

For independent experiments with a sample size $n \geq 3$, data were shown as means ± SD. Statistical differences were calculated through GraphPad Prism (version 9.0.0) using two-tailed unpaired student's *t*-test, and denoted as n.s., not significant, $^{*}P < 0.05$, $^{**}P < 0.01$, $^{***}P < 0.001$, and $^{****}P < 0.0001$. All flow cytometry data were analyzed on FlowJo™ software package (version 10.5.2). Quantitative analyses of H&E and fluorescence images were performed using image J software (version 1.8.0). Bioluminescent and fluorescent images were analyzed on CleVue (version 3.1.3.2054).

Reporting summary

Further information on research design is available in the Nature Portfolio Reporting Summary linked to this article.

Data availability

The authors declare that the data supporting the findings of this study are available within the Article, Source Data, and its Supplementary Information. The raw data generated for the RNA-seq analysis are available from the NCBI SRA database under the accession code PRJNA1194209. A reporting summary for this article is available as a Supplementary Information file. Source data are provided with this paper.

References

1. Peltonen, M. & Carlsson, L. M. Body Fatness and Cancer. *N. Engl. J. Med.* **375**, 2007–2008 (2016).
2. Powell-Wiley, T. M. et al. Obesity and Cardiovascular Disease: A Scientific Statement From the American Heart Association. *Circulation* **143**, e984–e1010 (2021).
3. Ladher, N., Hinton, R. & Veitch, E. Challenges of obesity and type 2 diabetes require more attention to food environment. *BMJ* **383**, 2269 (2023).
4. Wang, H., Liu, L., Lin, J. Z., Aprahamian, T. R. & Farmer, S. R. Browning of White Adipose Tissue with Roscovitine Induces a Distinct Population of UCP1(+) Adipocytes. *Cell Metab.* **24**, 835–847 (2016).
5. Scheja, L. & Heeren, J. The endocrine function of adipose tissues in health and cardiometabolic disease. *Nat. Rev. Endocrinol.* **15**, 507–524 (2019).
6. Li, Y. et al. Local hyperthermia therapy induces browning of white fat and treats obesity. *Cell* **185**, 949–966.e19 (2022).
7. Tsagkaraki, E. et al. CRISPR-enhanced human adipocyte browning as cell therapy for metabolic disease. *Nat. Commun.* **12**, 6931 (2021).
8. Cannon, B. & Nedergaard, J. Brown adipose tissue: function and physiological significance. *Physiol. Rev.* **84**, 277–359 (2004).
9. Bartelt, A. & Heeren, J. Adipose tissue browning and metabolic health. *Nat. Rev. Endocrinol.* **10**, 24–36 (2014).
10. Nicholls, D. G. The hunt for the molecular mechanism of brown fat thermogenesis. *Biochimie* **134**, 9–18 (2017).

11. Chouchani, E. T., Kazak, L. & Spiegelman, B. M. New Advances in Adaptive Thermogenesis: UCP1 and Beyond. *Cell Metab.* **29**, 27–37 (2019).
12. Neschen, S. et al. Uncoupling protein 1 expression in murine skeletal muscle increases AMPK activation, glucose turnover, and insulin sensitivity in vivo. *Physiol. Genom.* **33**, 333–340 (2008).
13. Tews, D. et al. Elevated UCP1 levels are sufficient to improve glucose uptake in human white adipocytes. *Redox Biol.* **26**, 101286 (2019).
14. Jagtap, U. & Paul, A. UCP1 activation: Hottest target in the thermogenesis pathway to treat obesity using molecules of synthetic and natural origin. *Drug Discov. Today* **28**, 103717 (2023).
15. Zhang, H. et al. Application of the CRISPR/Cas9-based gene editing technique in basic research, diagnosis, and therapy of cancer. *Mol. Cancer* **20**, 126 (2021).
16. Li, T. et al. CRISPR/Cas9 therapeutics: progress and prospects. *Signal Transduct. Target Ther.* **8**, 36 (2023).
17. Gilbert, L. A. et al. CRISPR-mediated modular RNA-guided regulation of transcription in eukaryotes. *Cell* **154**, 442–451 (2013).
18. Matharu, N. et al. CRISPR-mediated activation of a promoter or enhancer rescues obesity caused by haploinsufficiency. *Science* **363**, eaau0629 (2019).
19. Zheng, Q. et al. Reconstitution of UCP1 using CRISPR/Cas9 in the white adipose tissue of pigs decreases fat deposition and improves thermogenic capacity. *Proc. Natl. Acad. Sci. USA* **114**, E9474–E9482 (2017).
20. Wang, C. H. et al. CRISPR-engineered human brown-like adipocytes prevent diet-induced obesity and ameliorate metabolic syndrome in mice. *Sci. Transl. Med.* **12**, eaaz8664 (2020).
21. Mitchell, M. J. et al. Engineering precision nanoparticles for drug delivery. *Nat. Rev. Drug Discov.* **20**, 101–124 (2021).
22. Gillmore, J. D. et al. CRISPR-Cas9 In Vivo Gene Editing for Transthyretin Amyloidosis. *N. Engl. J. Med.* **385**, 493–502 (2021).
23. Wang, D., Zhang, F. & Gao, G. CRISPR-Based Therapeutic Genome Editing: Strategies and In Vivo Delivery by AAV Vectors. *Cell* **181**, 136–150 (2020).
24. Li, Y. et al. Encapsulation of Plasmid DNA by Nanoscale Metal-Organic Frameworks for Efficient Gene Transportation and Expression. *Adv. Mater.* **31**, e1901570 (2019).
25. Huang, Y. et al. A bimetallic nanoplatform for STING activation and CRISPR/Cas mediated depletion of the methionine transporter in cancer cells restores anti-tumor immune responses. *Nat. Commun.* **14**, 4647 (2023).
26. Liang, S. et al. Conferring Ti-Based MOFs with Defects for Enhanced Sonodynamic Cancer Therapy. *Adv. Mater.* **33**, e2100333 (2021).
27. Chen, R. et al. Photoacoustic molecular imaging-escorted adipose photodynamic-browning synergy for fighting obesity with virus-like complexes. *Nat. Nanotechnol.* **16**, 455–465 (2021).
28. Boussif, O. et al. A versatile vector for gene and oligonucleotide transfer into cells in culture and in vivo: polyethylenimine. *Proc. Natl. Acad. Sci. USA* **92**, 7297–7301 (1995).
29. Tenzer, S. et al. Rapid formation of plasma protein corona critically affects nanoparticle pathophysiology. *Nat. Nanotechnol.* **8**, 772–781 (2013).
30. Zhang, Y. et al. Scarless wound healing programmed by core-shell microneedles. *Nat. Commun.* **14**, 3431 (2023).
31. Zhao, M. et al. Ultrathin 2D Metal-Organic Framework Nanosheets. *Adv. Mater.* **27**, 7372–7378 (2015).
32. Ma, J., Bai, W. & Zheng, J. Non-enzymatic electrochemical hydrogen peroxide sensing using a nanocomposite prepared from silver nanoparticles and copper (II)-porphyrin derived metal-organic framework nanosheets. *Mikrochim Acta* **186**, 482 (2019).
33. Liang, S. et al. Harnessing Nanomaterials for Cancer Sonodynamic Immunotherapy. *Adv. Mater.* **35**, e2211130 (2023).
34. Guak, H. et al. PGC-1β maintains mitochondrial metabolism and restrains inflammatory gene expression. *Sci. Rep.* **12**, 16028 (2022).
35. Lee, J. M. et al. The E3 ubiquitin ligase TRIM25 regulates adipocyte differentiation via proteasome-mediated degradation of PPARγ. *Exp. Mol. Med*, **50**, 1–11 (2018).
36. Carling, D., Mayer, F. V., Sanders, M. J. & Gamblin, S. J. AMP-activated protein kinase: nature's energy sensor. *Nat. Chem. Biol.* **7**, 512–518 (2011).
37. Poher, A. L. et al. Ectopic UCP1 Overexpression in White Adipose Tissue Improves Insulin Sensitivity in Lou/C Rats, a Model of Obesity Resistance. *Diabetes* **64**, 3700–3712 (2015).
38. Bond, L. M. & Ntambi, J. M. UCP1 deficiency increases adipose tissue monounsaturated fatty acid synthesis and trafficking to the liver. *J. Lipid Res.* **59**, 224–236 (2018).
39. Nutter, S. et al. Changing the global obesity narrative to recognize and reduce weight stigma: A position statement from the World Obesity Federation. *Obes. Rev.* **25**, e13642 (2024).
40. Stanford, F. C. A new era in obesity management. *Nat. Rev. Gastroenterol. Hepatol.* **21**, 80-81 (2024).
41. Stefan, N., Häring, H. U. & Schulze, M. B. Metabolically healthy obesity: the low-hanging fruit in obesity treatment. *Lancet Diab. Endocrinol.* **6**, 249–258 (2018).
42. Heymsfield, S. B. & Wadden, T. A. Mechanisms, Pathophysiology, and Management of Obesity. *N. Engl. J. Med.* **376**, 254–266 (2017).
43. Perdomo, C. M., Cohen, R. V., Sumithran, P., Clément, K. & Frühbeck, G. Contemporary medical, device, and surgical therapies for obesity in adults. *Lancet* **401**, 1116–1130 (2023).
44. Abbasi, J. Semaglutide's Success Could Usher in a "New Dawn" for Obesity Treatment. *JAMA* **326**, 121–123 (2021).
45. Chouchani, E. T. et al. Mitochondrial ROS regulate thermogenic energy expenditure and sulfenylation of UCP1. *Nature* **532**, 112–116 (2016).
46. Mills, E. L. et al. Accumulation of succinate controls activation of adipose tissue thermogenesis. *Nature* **560**, 102–106 (2018).
47. Deligonul, F. Z., Yousefian, F. & Gold, M. H. Literature review of adverse events associated with cryolipolysis. *J. Cosmet. Dermatol* **22**, 31–36 (2023).
48. Jalian, H. R., Avram, M. M., Garibyan, L., Mihm, M. C. & Anderson, R. R. Paradoxical adipose hyperplasia after cryolipolysis. *JAMA Dermatol* **150**, 317–319 (2014).
49. Sakers, A., De Siqueira, M. K., Seale, P. & Villanueva, C. J. Adipose-tissue plasticity in health and disease. *Cell* **185**, 419–446 (2022).
50. Wu, Y. et al. PPA1 promotes adipogenesis by regulating the stability of C/EBPs. *Cell Death Differ.* **31**, 1044–1056 (2024).
51. Zhang, C. et al. Hyaluronic acid modulates gut microbiota and metabolites relieving inflammation: A molecular weight-dependent study. *Sci. Bull.* **69**, 2683–2687 (2024).

Acknowledgements

This work supported by the National Nature Science Foundation of China grant to L.P.S. (82171945), H.X.X. (82151318, 82430064 and 81927801), Y.F (82102050), and H.H.Y. (82302206), Shanghai Municipal Health Commission grant to H.X.X. (SHSLCZDZK03502), Scientific Research and Development Fund of Zhongshan Hospital of Fudan University grant to H.X.X. (2022ZSQD07), Shanghai Sailing Program to H.H.Y. (23YF1441600) and China Postdoctoral Science Foundation to H.H.Y. (2023TQ0073).

Author contributions

L.P.S., H.X.X., H.H.Y., and S.Y.L. designed the research strategy; S.Y.L., H.H.Y., J.F.Y., Y.T.S., B.X., D.Z., W.C.X., S.Z., X.G., Y.Y.L., X.X.S., A.Q.Z., Q.L., Y.F., and Z.T.C. performed experiments and/or analyzed the data; S.Y.L. and H.H.Y. wrote the paper; L.P.S., H.X.X., and H.H.Y. supervised the whole process.

Competing interests
The authors declare no competing interests.

Additional information
Supplementary information The online version contains supplementary material available at https://doi.org/10.1038/s41467-025-56755-4.

Correspondence and requests for materials should be addressed to Haohao Yin, Liping Sun or Huixiong Xu.

Peer review information *Nature Communications* thanks the anonymous reviewer(s) for their contribution to the peer review of this work. A peer review file is available.